Chair of Polymer Processing

Master's Thesis

Fabrication of multi-material dielectric elastomer actuators with the additive manufacturing process of material extrusion

Philipp Beier, BSc

May 2024

MONTANUNIVERSITÄT LEOBEN
www.unileoben.ac.at

AFFIDAVIT

I declare on oath that I wrote this thesis independently, did not use any sources and aids other than those specified, have fully and truthfully reported the use of generative methods and models of artificial intelligence, and did not otherwise use any other unauthorized aids.

I declare that I have read, understood and complied with the "Good Scientific Practice" of the Montanuniversität Leoben.

Furthermore, I declare that the electronic and printed versions of the submitted thesis are identical in form and content.

Date 14.05.2024

Signature Author
Philipp Beier

Acknowledgement

First and foremost, I express my gratitude to Univ.-Prof.- Dipl.-Ing. Dr.mont. Clemens Holzer for granting me the opportunity to conduct my Thesis at the Chair of Polymer Processing.

I would like to express gratitude to Dipl.-Ing. Stephan Schuschnigg and Ivan Raguž, MSc. for their invaluable help during my work.

Furthermore, I would like to extend thanks to my colleagues, particularly Julia Lipowsky, for helping during the experimental phase of my thesis.

Abstract

Dielectric elastic actuators (DEA) are versatile devices with various applications, such as in the field of soft robotics or sensor measurement technology. Additive manufacturing (AM) enables the production of various materials with complex geometries in a layer-by-layer process and Material extrusion (MEX) is a highly promising subcategory of it. In this process, filaments are utilised and passed through an extruder to create the component in a sequential manner, layer by layer. There are various methodologies for producing parts made of multiple materials. This study employed a multi-extruder approach to address the issues associated with processing soft materials that are difficult to handle. Materials that contain additives like graphite can potentially contaminate the nozzle, resulting in increased difficulty when attempting to clean it.

Therefore, a novel tool was developed to manage four extruders on a single axis. Moreover, they were mounted on two separate movable carriages, each capable of accommodating two extruders. Dual extruders have become well-established in the industry and are widely used in the commercial sector. It is an efficient and simple method to simultaneously process two materials in a single print. In order to verify the precision and consistency of the custom printer, various measurements were performed, including capacitance and the overall thickness of the produced parts. The machine was required to reliably produce layers with a height of 70 µm. The deviation reached a maximum of 8 %, which is a commendable outcome considering the limitations of the hardware.

Another section of the thesis focused on the analysis of various types of polyurethanes (TPU) for the purpose of DEAs. The study examined the impact of varying shore hardness levels and printing orientations on material selection. The investigation revealed that using an infill orientation of either 0° or 90° yielded similar values for both the Young's modulus and flexural modulus. This can be attributed to the seamless melding of the strings, resulting in minimal differences between orientations. Regarding the shore hardness of the materials, they exhibited comparable bending stiffness across a range of 83A to 20D. A significant increase of over 200 % in the Young's modulus was observed only when the hardness reached 40D. The moduli of the TPUs used as electric conductive materials were even higher. This phenomenon may be attributed to the graphite particles, which embed themselves within the gaps in the chains, thereby enhancing the material's rigidity.

The DEAs that were produced underwent displacement measurements to determine their functionality. As anticipated following the mechanical test, all actuators exhibited comparable displacements. The findings suggest that the capacitance of the actuator is the main factor influencing the result. When the capacitance is decreased, the displacement is proportionally reduced. Based on the actuators that were tested, a prototype application was designed and manufactured. Three actuators were linked in parallel and served as gripping arms.

Kurzfassung

Die dielektrischen elastischen Aktuatoren (DEA) sind vielseitige Geräte für verschiedenen Anwendungen, wie zum Beispiel auf dem Gebiet der Soft Robotik oder der Sensormesstechnik. Die additive Fertigung (AM) ermöglicht die Herstellung unterschiedlichen Materialien mit komplexen Geometrien in einem Schicht-für-Schicht-Prozess und Material-Extrusion (MEX) ist eine vielversprechende Unterkategorie davon. In diesem Prozess werden Filamente genutzt und durch einen Extruder geführt, um die Komponente auf sequenzielle Weise, Schicht für Schicht, zu drucken. Es gibt verschiedene Methoden zur Herstellung von Bauteilen aus mehreren Materialien. In dieser Studie wurde ein Multi-Extruder-Ansatz gewählt, um die Herausforderung der Verarbeitung von weichen Materialien und der Reinigung der Düsen aufgrund der Anwesenheit von Zusatzstoffen wie Grafit notwendig zu meistern.

Daher wurde ein neues Werkzeug entwickelt, um vier Extruder auf einer einzelnen Achse zu verwalten. Darüber hinaus wurden sie auf zwei getrennten beweglichen Halterungen montiert, die jeweils zwei Extrudern aufnehmen konnten. Doppel-Extruder haben sich in der Industrie etabliert und sind im kommerziellen Sektor weit verbreitet. Es ist eine effiziente und einfache Methode zur gleichzeitigen Verarbeitung von zwei Materialien in einem einzigen Druck. Um die Präzision und Konsistenz des selbstgebauten Druckers zu überprüfen, wurden verschiedene Messungen durchgeführt, einschließlich der Kapazität und der Gesamtdicke des hergestellten Bauteiles. Die Maschine musste zuverlässig Schichten mit einer Höhe von 70 µm herstellen. Die Abweichung erreichte maximal 8 %, was angesichts der Einschränkungen der Hardware ein gutes Ergebnis ist.

Ein weiterer Abschnitt der Arbeit konzentrierte sich auf die Analyse verschiedener Typen von Polyurethanen (TPU) für die Zwecke der DEA. Die Untersuchung zeigten die Auswirkungen unterschiedlicher Härtegrade und Druckorientierungen auf die Materialwahl. Die Experimente ergaben, dass die Verwendung einer Füllorientierung von entweder 0° oder 90° ähnliche Werte sowohl für das Young-Modul als auch für den Biegemodul hatten. Dies ist auf die nahtlose Verschmelzung der Stränge zurückzuführen, welche zu minimalen Unterschieden zwischen den Orientierungen führt. In Bezug auf den Härtegrad der Materialien zeigten sich vergleichbare Biegesteifigkeiten im Bereich von 83A bis 20D. Eine signifikante Zunahme von über 200 % im Young-Modul wurde nur beobachtet, wenn die Härte 40D erreichte. Die Module der TPUs, die als elektrisch leitfähige Materialien verwendet wurden, waren noch höher. Dieses Phänomen kann den Graphitpartikeln zugeschrieben werden, die sich innerhalb der Lücken in den Ketten einbinden, wodurch die Festigkeit des Materials erhöht wird.

Mit den hergestellten DEAs unterzogen sich Verschiebungsmessungen, um ihre Funktionalität zu bestimmen. Wie nach dem mechanischen Test erwartet, zeigten alle Aktautoren vergleichbare Verschiebungen. Die Ergebnisse deuten darauf hin, dass die Kapazität des Aktuators der Hauptfaktor ist, der das Ergebnis beeinflusst. Wenn die Kapazität abnimmt, wird die Verschiebung proportional reduziert. Basierend auf den getesteten DEAs wurde eine Prototypenanwendung entworfen und hergestellt. Drei Aktuatoren wurden parallel miteinander verbunden und dienten als Greifarm.

Table of Contents

1 Introduction

Dielectric elastomer actuators (DEA) are a class of intelligent material systems, that have the capability to generate significant strains and have a notable elastic energy density [79]. The essential constituents of a DEA consist of an elastomeric material serving as the dielectric, bordered on either side by electrically conductive material acting as electrodes. The contraction in thickness of the elastomer is a result of Coulomb forces, leading to expansion in other dimensions upon the application of an electrical voltage between the electrode layers [25, 86, 88]. In the case of a symmetrical DEA configuration, it leads to an expansion in the projected surface area. Deformation typically manifests in formations that lack symmetry. The occurrence of this phenomenon might be attributed to either variations in geometric factors or the utilization of different materials.

The objective of this study was to develop soft dielectric actuators through the utilisation of commercially accessible filaments and printers, using a fully 3D-printed approach. The object was to produce a dielectric elastomer actuator using a single manufacturing process, incorporating a minimum of four layers composed of three distinct materials. Considerable investigation has been undertaken with soft dielectric actuators featuring partially additively made dielectric elastomer actuators [41, 78]. This study explores the boundaries of the Material Extrusion (MEX) Additive Manufacturing (AM) method in order to fabricate fully functional actuators that are suitable for practical use. Currently, there is a restricted range of filaments for electrically conductive materials compatible with material extrusion technology and commercially accessible. The selection of the MEX printing technology was based on its ability to provide readily accessible multi-material printing, which is essential for the continuous and unified production of DEAs. Soft robots exhibit potential as viable contenders for the initial deployment of partially or fully 3D-printed robots, namely those encompassing dielectric elastomer actuators that are exclusively fabricated by 3D printing techniques [40].

Flexible filaments pose a specific challenge when it comes to processing. On one hand, they tend to become entangled with the driver gears in the extruder when the pressure gets too high. On the other hand, this can also occur if the gears used do not have sufficient grip to feed the filament into the nozzle properly. Therefore, it is crucial to use special extruders with larger driver gears to ensure a better contact surface. This allows sufficient pressure to be applied to the filament, ensuring reliable feeding.

When employing multi-material approaches in material extrusion, there are typically two methods: utilizing a single extruder fed through a multi-material unit or using a multi-extruder setup [81]. The first method has notable drawbacks when dealing with flexible or highly filled filaments. The existing systems are tailored for robust and easily feedable extruders. If the filament becomes excessively soft, the system will fail to guide the filament into the extruder effectively. Another issue with using a single extruder is the contamination of the nozzle when using electrically conductive filaments [20, 94]. They are typically filled with graphite or soot and can modify the characteristics of other materials being used. Printing actuators with contaminated material can reduce the dielectric properties of the dielectric material. Purging a large amount of material before resuming printing to clean the nozzle is possible, but not very efficient and time-consuming. The most practical approach is to utilise a multi-extruder setup. Although dual extruders are common, using additional ones remains difficult. A common method involves using a tool change mechanism, where extruders are stationed at the rear of the printer and only the active extruder moves along the extruder axis (typically the y-axis on

Cartesian printers) [48, 56]. This method is highly complex and presents several challenges. The precise mounting of the extruder during each tool change is currently unreliable for producing extremely accurate parts. Nevertheless, the main issue lies in the high price of tool change equipment and the necessity for proficient coding to ensure optimal functionality.

Consequently, a determination was reached to develop a printer featuring two dual extruder configurations capable of independent movement along the y-axis. This approach is economically efficient and mitigates problems arising from inaccuracies in the extruder's mounting during tool changes.

Another area of focus in this study involved conducting material tests using existing filaments for the manufacturing of actuators. The key features of these filaments include their processability and compatibility, particularly the adhesion between distinct materials. Additional characteristics related to their role in the actuator were also examined. The evaluation involves an analysis of mechanical properties, specifically the Young’s modulus and the poison ratio, within the passive layer of the actuator. The dielectric constant was measured for the dielectric component. The evaluation of capacitance and the assessment of actuator thickness are crucial in determining the precision and dependability of the custom 3D printer.

The final phase of the study involved creating a device in the shape of a three-finger actuator that serves as a gripping arm. This could demonstrate potential applications for this type of devices. The geometry displayed similarities to the DEA's that were designed for analysis purposes. This processing technique has the capacity to generate a wide variety of potential applications.

2 Theoretical Background

2.1 Additive Manufacturing

The EN ISO/ASTM 52900 [2] standard defines additive manufacturing as "process of joining materials to make parts from 3D model data, usually layer upon layer, as opposed to subtractive manufacturing and formative manufacturing methodologies" [28]. Additive manufacturing is an umbrella term for a variety of manufacturing techniques that permit the fabrication of a three-dimensional object from a digital model [36]. The data is extracted from a computer-aided design (CAD) file or a digital scan and transformed into a Standard Triangulation Language (STL) or an Additive Manufacturing File Format (AMF) file. This is inserted into a program called a "slicer" and sliced into thin layers [19]. The print head's movements are then calculated for each layer. Comparable to a conventional 2D printer, a 3D printer "prints" each of these layers. Therefore, the component is constructed layer by layer. Various AM technologies can process various materials (e.g. plastics, metals or ceramics).

2.1.1 Material Extrusion

Material extrusion (MEX) is an additive manufacturing process, in which polymeric filaments are used to construct the component. The filament is extruded through a heated die during this procedure [13]. The company Stratasys commercialised the process in the 1980s under the registered trademark name FDM™ (Fused Deposition Modeling™). The fundamental patents for the process have since expired, and the term "Material Extrusion" has since been used. This process requires relatively basic equipment, so a variety of affordable machines and kits are now available for home users. In addition, the MEX process is significantly more environmentally friendly than other AM processes that use granules, powders, or liquids [12]. Figure 1 depicts the configuration of a MEX system. The filament is wound on a spool, guided into an extruder. Within the hotend, the filament is melted, resulting in the extrusion of a viscous plastic melt through the nozzle. Using an x-y drive, the nozzle is moved over the build platform, and a filament of molten material is deposited on it. After each layer, the platform is lowered by the thickness of one layer in the z-direction. For particularly large components, there are also devices with a fixed build platform and an upwardly moving nozzle head. In more advanced machines, the construction area is tempered to improve the bond between the molten filament and the deposited strands.

The majority of MEX printers utilize a build plate comprised of glass or diverse polymers [17]. The objective is to guarantee uniform adhesion across the entire build plate. In practice, however, constant adhesion is not attained; therefore, several methods are recommended for enhancing adhesion [59, 95]:

(i) Residue-free cleaning of the construction plate.

(ii) Calibration of the first layer so that the nozzle is positioned at the correct distance from the build plate.

(iii) Using water-soluble adhesives or adhesion promoters.

(iv) Increasing the temperature of the construction plate, above the material's recommended temperature.

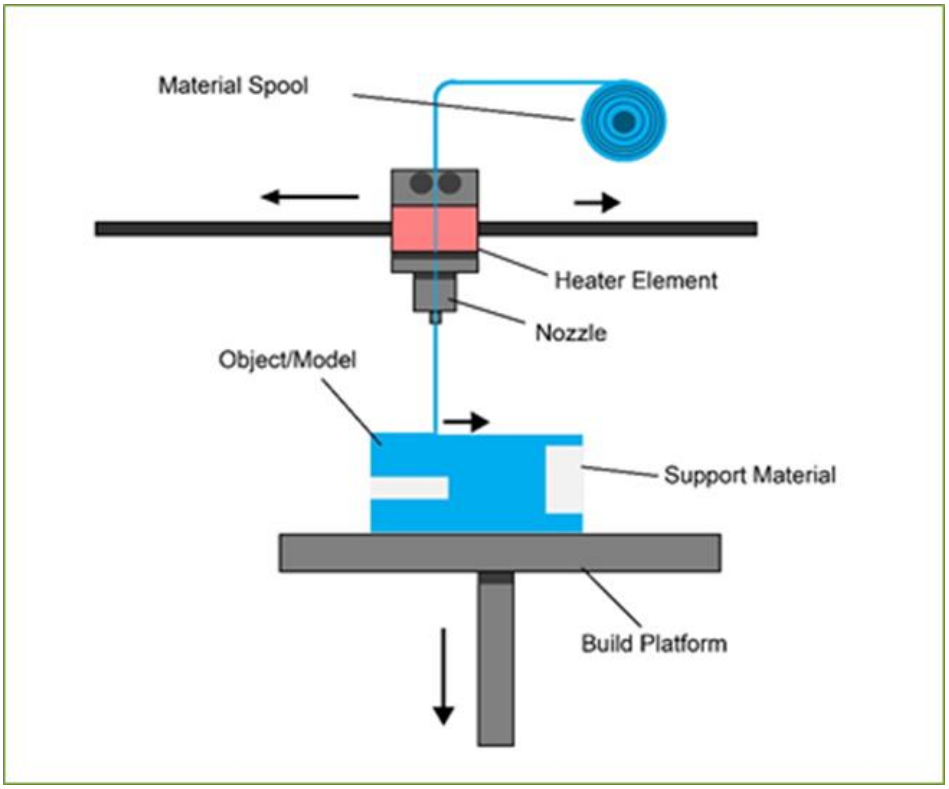

Figure 1: Basic design of a MEX [67]

The MEX processing method can be classified into four distinct types of kinematic motions, each with its own advantages and disadvantages:

2.1.2 Cartesian Printer

Cartesian printers feature a minimum of three motors that control the movement of printer components along the Y-axis (back and forth), X-axis (left and right), and Z-axis (up and down) of the Cartesian coordinate system (Figure 2). Cartesian printers are the most common type of personal desktop printer because they are widely available and inexpensive [90, 101].

Cartesian printers may produce lower-quality prints when used at higher speeds, due to the weight of the axes. Typically, the printer volume exceeds the build volume significantly because of the motion across all axes [101, 103].

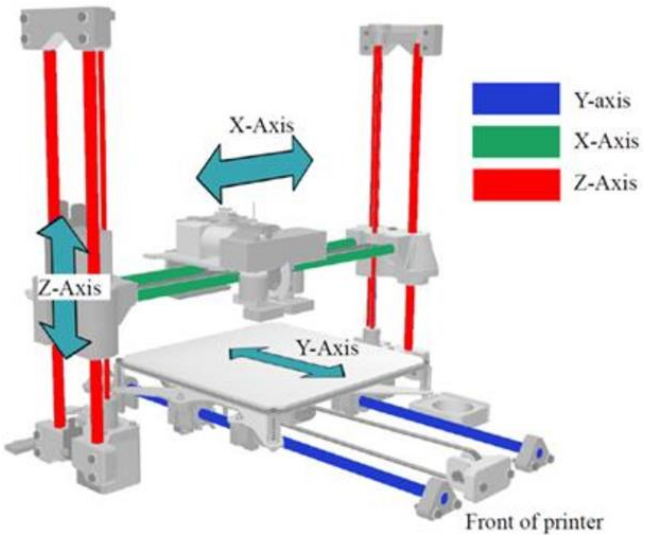

Figure 2: Illustration of kinematic movement of a Cartesian printer [85].

2.1.3 Core XY Printer

The Core XY design, similar to Cartesian printers, utilises two motors and timing belts on the X and Y axes to determine latitudinal and longitudinal coordinates, while the Z-axis controls the print height. The Core XY operates through interdependent X and Y movements facilitated by a unique belt design (Figure 3). In this scenario, the print surface will be raised to align with the extruder [85]. The design maximises the build volume by eliminating the need for the print surface to move sideways. Furthermore, the lighter axis allows for faster printing compared to Cartesian printers [101].

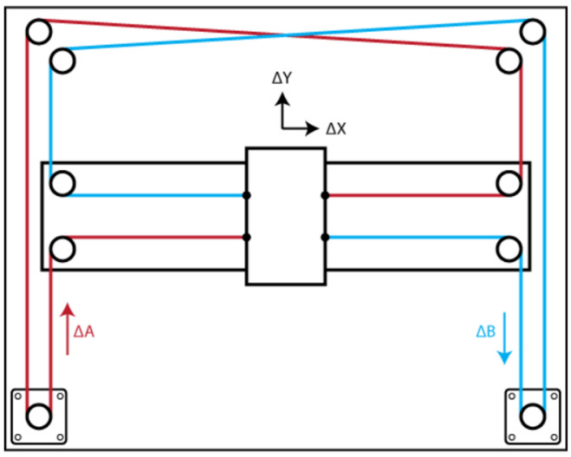

Figure 3: Reference mechanism of a CoreXY printer [21].

2.1.4 Delta Printer

The Delta architecture has the most distinct kinematics among the three. Three motors, one in each tower, work collectively to move the X, Y, and Z axes vertically, as shown in Figure 4. This design is simple, utilising only three motors for motion instead of the typical four [85]. The printer was one of the first to use a 32-bit system because of the intricate calculations required for its movements.

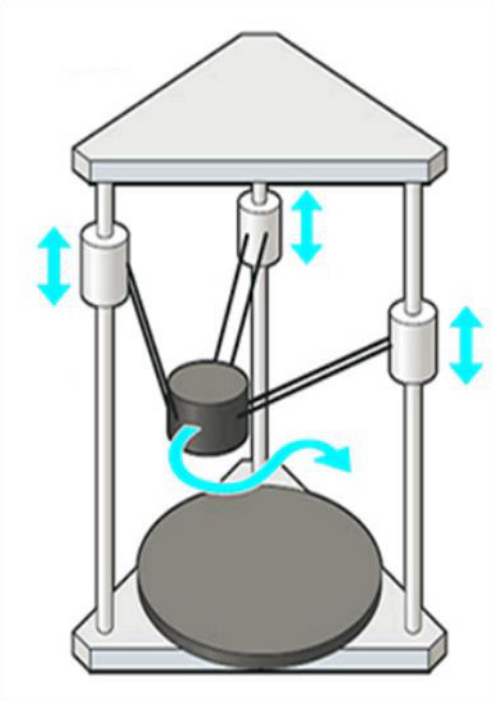

Figure 4: Schematic of Delta printer [101].

2.1.5 Bowden Extruder

The Bowden extruder is a type of extrusion mechanism in which the extruder is physically separated from the printhead and typically attached to the printer's frame (shown in Figure 5a). The filament is fed through a PTFE (polytetrafluoroethylene) tube by the extruder. The tube serves the purpose of maintaining the stability of the filament during its introduction into the printhead. [30, 46]

The reduced mass of the carriage can greatly enhance the printing velocity, in contrast to a direct extruder configuration. Additionally, reduced vibration on the extruder axis can result in improved print quality [46].

2.1.6 Direct Extruder

In the direct extruder configuration, the extruder is mounted directly onto the printhead (shown in Figure 5b), enabling the filament to be fed straight into the printhead. The enhanced filament control achieved through the close proximity of the extruder and the nozzle leads to a more consistent extrusion or retraction process. This is especially crucial when using flexible or brittle filaments [30, 46].

One notable drawback associated with a direct extruder is the substantial weight added to the axis when mounting the extruder onto the printhead. This weight can have an impact on both the print quality and the maximum print speed [46].

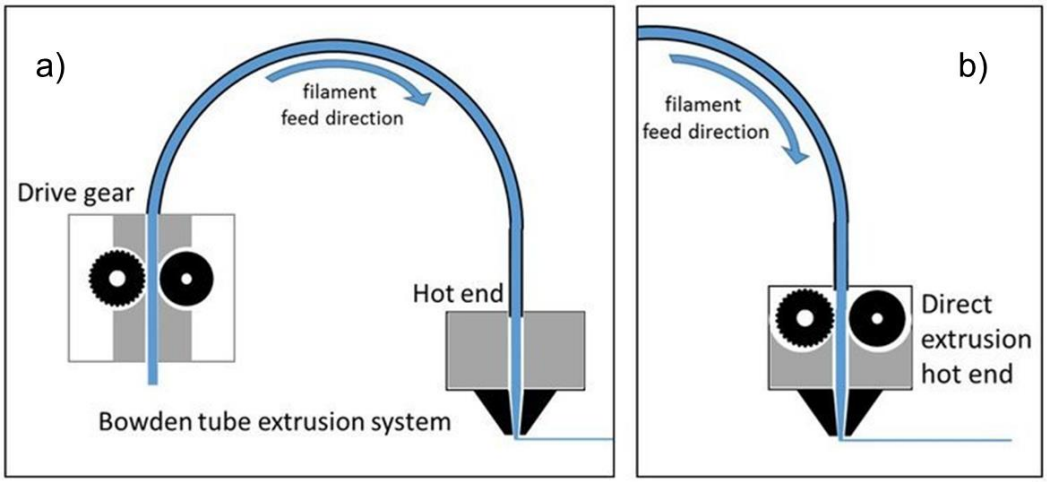

Figure 5: Extruder configuration: a) Bowden extruder, b) direct extruder [10].

2.2 Thermoplastic Elastomer

Thermoplastic elastomers (TPEs) are composite materials consisting of two distinct phases, namely a hard and a soft component. When used in applications, these materials show elastomeric behaviour but can also function as thermoplastic polymers when subjected to high temperatures during processing. These two phases have well-defined transitional zones. The elastomeric features of the material are attributed to the soft component, which serves to connect the hard components. In contrast, the hard component forms a network that is not permanent and can be broken at elevated temperatures (i.e. by melting). Permanently cross-linked elastomers cannot be plasticized after vulcanization. There are two techniques to make thermoplastic elastomers: the block copolymerization of hard and soft segments in the reactor or the mixing of incompatible thermoplastic and elastomer polymer blends [49, 91].

Various thermoplastic elastomers are classified according to the standard DIN EN ISO 18064:2022-08 [26], as shown in Figure 6.

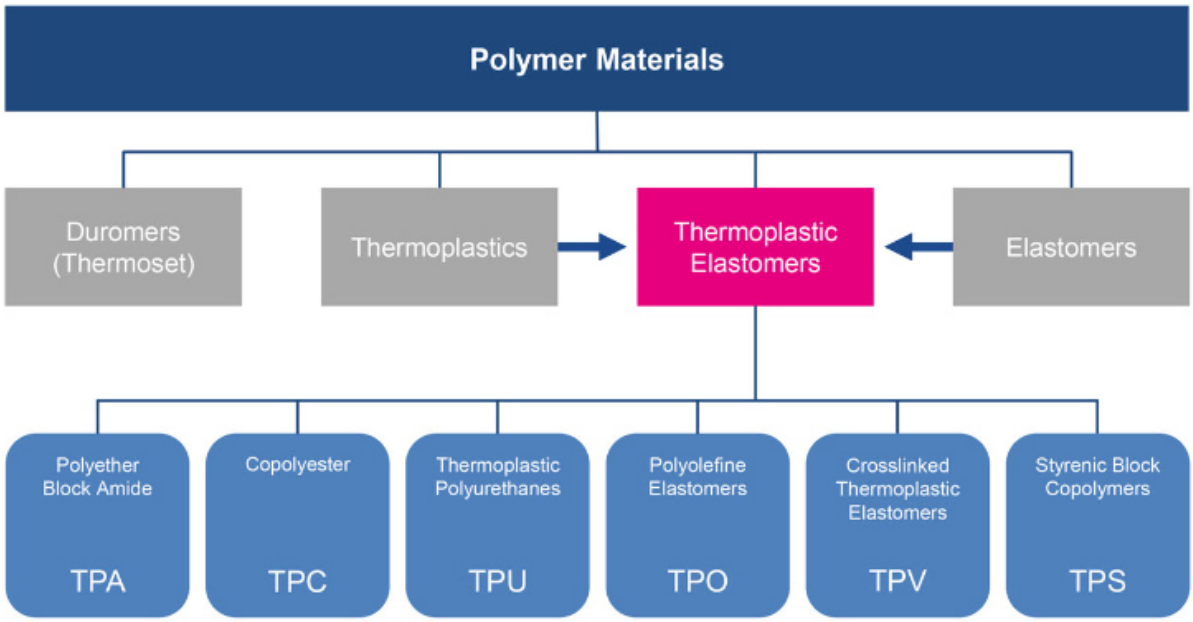

Figure 6: Classification of various types of Thermoplastic Elastomers according to DIN EN ISO 18064:2022-08 [102].

Thermoplastic polyurethane (TPU) in particular, is a polymer material that can be processed through additive manufacturing. It possesses high ductility, good resistance to hydrolysis, excellent biocompatibility, and strong abrasion resistance [7, 61, 69]. It is suitable for use in structures that demand high ductility, such as energy-absorbing structures and wearable devices [8, 89].

TPUs are block copolymers composed of soft segments (SS) and hard segments (HS) that demonstrate phase separation [66, 96]. This uniqueness arises from the various types of cross-linkages present in its structure. A single monomer creates rigid, crystalline regions that offer thermal stability and soften under shear stress without relying on chemical cross-links, as seen in conventional thermosetting rubber. The second monomer forms the soft, non-crystalline areas responsible for the material's rubber-like characteristics [23]. Various factors affect phase separation, including variations in segmental polarity, segmental length, intra- and intersegment interactions like hydrogen bonding, overall composition, and molecular weight [70]. The HS is usually composed of a stiff diisocyanate and a chain extender such as a diol, while the SS primarily contains a lengthy polyol.

These systems typically separate into microphases or domains. TPUs' physical characteristics are influenced by the extent and configuration of phase separation, which is closely linked to HS content [24, 43].

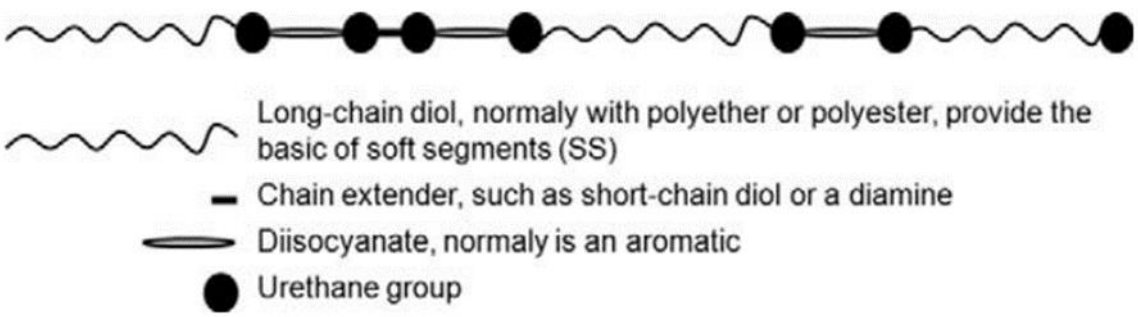

Figure 7: Schematic representation of a segmented TPU copolymer [23].

2.3 Dielectric Elastomer Actuator

2.3.1 Working Principle

Interest in dielectric elastomer actuators (DEAs) has grown in recent decades. The possibility of creating or imitating natural muscle structure in a lightweight and uncomplicated manner is the rationale behind it [29, 51]. The basic actuator setup is similar to a parallel plate capacitor and involves a thin elastomer sheet placed between two conducting electrodes that can be charged with a potential. DEAs are devices that transform electrostatic energy, derived from an external electric potential, into strain energy and mechanical work by deforming a soft dielectric material (shown in Figure 8) [42, 87].

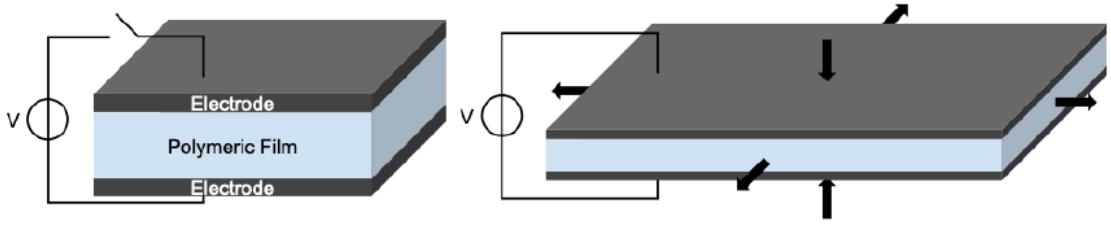

Figure 8: Illustration of a dielectric elastomer actuator [32]

When connected to a power supply, one electrode is positively charged, and the other is negatively charged. Opposite charges create a net Coulombic attraction that results in a compressive force. The polymeric film is compressed in thickness and elongated in length and width due to electrostatic forces. [45, 87]

The electrostatic force on the flexible membrane is related to the driving voltage U, the distance between the compliance electrodes d, and the surface area between the electrodes A [104]. The formula for the electrostatic force of the flexible membrane is denoted as F_e.

$$F_e = \frac{1}{2}\varepsilon\left(\frac{U}{d}\right)^2 A = \frac{1}{2}\varepsilon U^2\left(\frac{1}{D_0 - w}\right)^2 A \quad (1)$$

Where the electric field constant is represented by ε_0, D_0 stands for the initial distance between the electrodes, and w indicates the displacement in the transverse z-direction. This actuation principle is referred to as two-axis planar actuation. The structure can expand in both the x and

y axes due to the strain caused by the high voltage (shown in Figure 9a). According to Bigue et al., the DEA has a constant membrane thickness and area, denoted as d and A respectively [11]. The film's volume ψ is constant and can be determined by the equation:

$$\psi = Ad \tag{2}$$

Structural deformation is caused by Maxwell stresses produced by electric charges situated on the electrodes. The total electrical charge Q, is situated on the electrodes of the film under the applied voltage U, as indicated by the following equation:

$$Q = CU \tag{3}$$

The actuator capacitance C can be determined using the flat plate capacitor equation provided below:

$$C = \epsilon_r \epsilon_0 \frac{A}{d} \tag{4}$$

where ϵ_0 represents the permittivity of free space and ϵ_r denotes the relative dielectric constant of the dielectric material. The Maxwell pressure, denoted as P, resulting from electrostatic attraction is defined by the following equation [60].

$$P = \varepsilon_r \epsilon_0 \left(\frac{U}{d}\right)^2 \tag{5}$$

Expansion and elongation happen in only one direction along the x- or y-axis in a one-axis planar actuation or a configuration with one fixed end (illustrated in Figure 9b). The bend-type actuation is characterised by a surface layer being constrained from moving, resulting in the structure warping towards the restricted surface (depicted in Figure 9c). With slight modifications, it is possible to configure various types of motion.

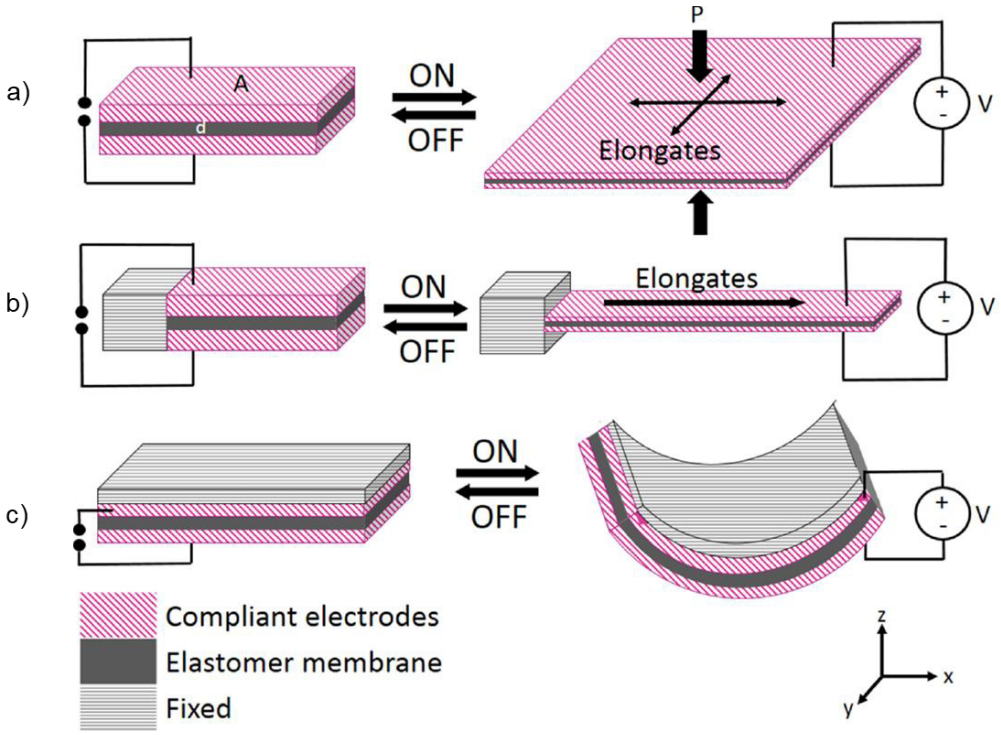

Figure 9: a) Two-axis planar actuator, b) One-axis planar actuator, c) bend actuator [60].

2.3.2 Dielectric Material

The properties of dielectric elastomer (DE) materials are crucial for the performance of DEA. For improved performance, the material must possess characteristics such as low modulus, low viscosity, high electrical breakdown strength, and a high dielectric constant [9]. Commonly used materials can be categorised into three groups: acrylics, silicones, and polyurethanes (PU's). Acrylic elastomers VHB 4910 and VHB 4905 from 3M Company are commonly used in experiments due to their commercial availability and low cost. They are capable of generating a higher voltage-induced strain, specifically a linear strain exceeding 380 % [79] and an area strain over 2200 % [80]. Silicone elastomers have a lower actuation strain compared to acrylic elastomers. A higher voltage is needed to achieve greater strain due to the lower dielectric constant. Silicone-based DEAs can operate at high frequencies due to their significantly lower viscoelasticity [16, 39]. PUs typically offer greater output force. A reduced electric field can operate DEAs utilising PUs because of the PU naturally higher dielectric constant. Nevertheless, the increased modulus leads to a relatively minor strain [44].

2.3.3 Compliant Electrodes

Compliant electrodes are another crucial element of DEAs that significantly impacts their functionality. The electrodes should possess high compliance, high conductivity, good stability, and strong adhesion to the membrane. Common compliant electrodes used in DEAs are carbon grease, carbon powder, carbon nanotubes (CNTs), and graphite [16, 18, 63, 76, 87]. Carbon grease is the most commonly used option due to its affordability, high flexibility, and widespread availability. Yet, the disadvantage of carbon grease is that the oil it contains will eventually evaporate over time. Carbon powder and graphite are preferable for multilayer stacked DEAs due to their ease of application on the membrane surface and their thinness.

Conductivity decreases when powders lose contact under increased strain. CNTs and silver nanowires (AgNWs) are utilized as compliant electrodes in adaptive optical devices because of their exceptional conductivity and transparency [58, 62, 93].

2.4 Plate Capacitor

2.4.1 Capacitance

A component's capacitance is its ability to store electrical energy. This characteristic is possessed by the capacitor. The capacitance between two conductors is solely a function of geometry. The opposing surface areas of the conductors, the distance between them, and the permittivity of any dielectric substance between them. The permittivity and capacitance of many dielectric materials are independent of the potential difference between the conductors and the total charge on them. The capacitance C is defined by the ratio of charge Q and electric potential U $[3, 3, 100]$:

$$C = \frac{Q}{U} \tag{6}$$

2.4.2 Force Acting on the Plates

The plates of a capacitor with different charges are attracted to each other as a result of Coulomb's law (Figure 10).

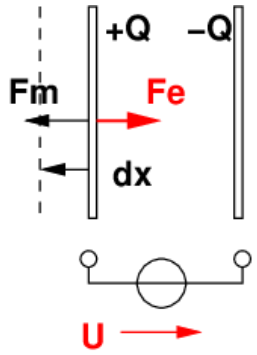

Figure 10: Derivation of the force on the plates of the capacitor [84].

When a charge Q is displaced against the electric field force $\vec{F}_e$, a mechanical force $\vec{F}_m$ is required to accomplish this.

$$\vec{F}_m = \vec{F}_e \tag{7}$$

The forces can be determined by applying the principle of energy conservation. When a plate is moved a short distance dx against the force F_m,

$$dW_m = F_m\, dx \tag{8}$$

mechanical energy dW_m is transferred to the capacitor as a conversion to electrical energy dW_e (The principle of virtual work).

$$dW_e = dW_m = F_m\, dx \tag{9}$$

Solving the mechanical force required to displace a plate result in the overall correlation [37].

$$F_m = \frac{dW_e}{dx} \tag{10}$$

The force in a plate capacitor is also determined by multiplying its electric charge by the electric field intensity E within the capacitor [97].

$$F_m = QE \tag{11}$$

The following applies to the electric field strength E between the capacitor plates,

$$E = \frac{U}{d} \tag{12}$$

where U represents the applied voltage and d is the distance between the plates.

This leads to the electrical work [100].

$$W_e = \frac{1}{2}QEd = \frac{1}{2}QU \tag{13}$$

When Q is constant and the energy of the voltage source remains unchanged, substituting equation (6) into equation (12) results in

$$dW_e = d\left(\frac{Q^2}{2C}\right) = \frac{Q^2}{2}d\left(\frac{1}{C}\right) \tag{14}$$

and for the mechanical force on the plates,

$$F_m = \frac{dW_e}{dx} = \frac{Q^2}{2}\frac{d}{dx}\left(\frac{1}{C}\right) = \frac{Q^2}{2}\frac{1}{\varepsilon A}\cdot\frac{d}{dx}(x) = \frac{Q^2}{2}\cdot\frac{1}{\epsilon A} \tag{15}$$

where ε represents the dielectric constant and A denotes the area of the plates.

2.5 Electric Resistance

Polymers typically have high electrical resistivities and are primarily used as insulators in electrical applications. Conductive grades have specific requirements, so base polymers are often altered to fulfil these requirements [12]. The volume resistivity ρ of an isotropic material is the resistance measured according to Ohm's law between opposite faces of a unit cube. The resistance R between the opposite ends of a block with uniform cross-sectional area A and length l is determined by [1, 13]:

$$R = \frac{\rho l}{A} \tag{16}$$

The generalized Ohm's law can express volume resistivity by utilizing the electric field E and current density J:

$$E = \rho J \tag{17}$$

The solid dielectric's conductivity is the inverse of its resistivity. To measure the resistance, the specimen is positioned between the conductive electrodes. The resistance value is determined by measuring the current passing through the sample at the voltage applied to the electrode. The value is influenced by the size of the electrode and the sample [57]. The surface resistivity can be determined using the three-terminal electrode measurement technique recommended by ASTM D 257 [99]. Figure 11 displays the measurement setup. It consists of three electrodes: top, bottom, and guard electrodes. Figure 11b depicts the test specimen and should be set up according to [57]:

$$D_0 = \frac{D_1 - D_2}{2} \tag{18}$$

D_0 is the distance from the origin to the midpoint of g, D_1 is the diameter of the bottom electrode, D_2 is the diameter of the bottom electrode plus g (spacing between the guard and bottom electrode), and D_3 is the diameter of the top electrode.

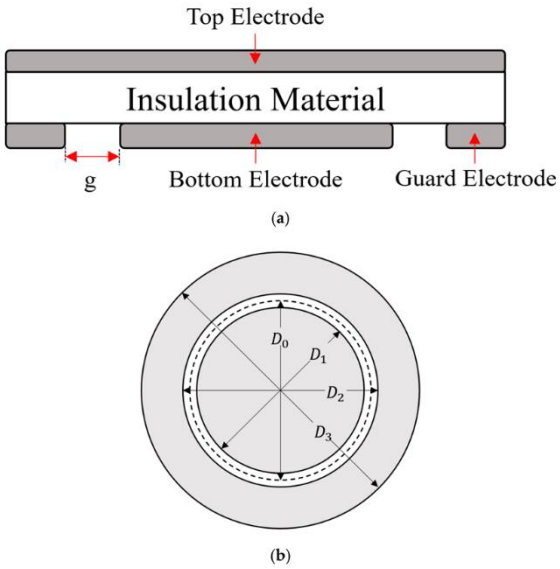

Figure 11: a) Measurement setup for resistance measuring and b) flat test specimen [57]

2.6 Tensile Testing

In a tensile test, a sample is clamped and subjected to an increasing tensile load until it fails, measuring the requisite force and distance from the machinery. From this, the modulus of elasticity and breaking stress can be calculated. Due to the limited elastic deformation range of plastics, the E-modulus is determined as the secant modulus (Figure 12 a). It includes the elastic and linear viscoelastic deformation ranges of the stress-strain curve [31, 38].

According to standard OENORM EN 527-2 [54], the tensile modulus, or Young's modulus Y is determined by the change in tension $\Delta\sigma$ and strain $\Delta\varepsilon$ (between 0.05 and 0.25 %):

$$Y = \frac{\sigma_2(\varepsilon_2 = 0{,}25\%) - \sigma_1(\varepsilon_1 = 0{,}05\%)}{\varepsilon_2 - \epsilon_1} = \frac{\Delta\sigma}{\Delta\varepsilon} \tag{19}$$

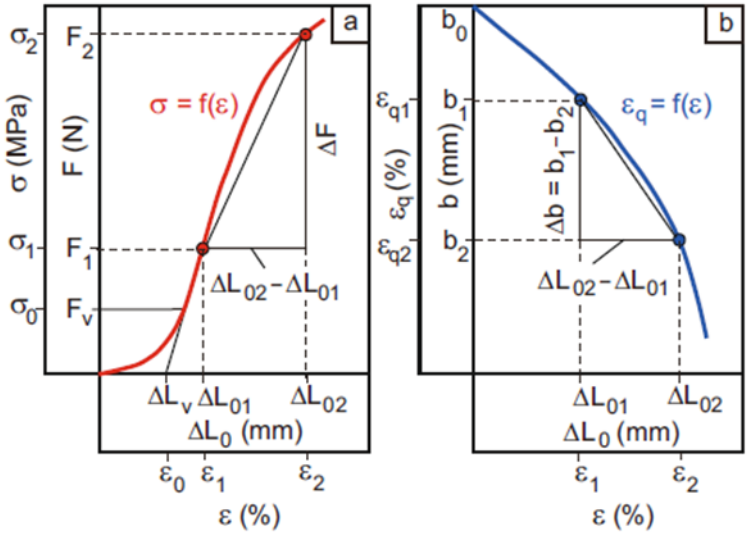

Figure 12: Determination of the elastic constants in the tensile test: a) stress-strain diagram, b) transverse strain-longitudinal strain diagram [38].

By using a second strain gauge that simultaneously detects the change in thickness, or preferably width, along with the longitudinal deformation, the Poisson's ratio μ_b (width) or μ_h (thickness) can also be measured (Figure 12 b). This elastic parameter is calculated as follows in the case of the width change [38]:

$$\mu_b = \left|\frac{\varepsilon_{qb}}{\varepsilon}\right| = \left|\frac{\Delta b L_0}{\Delta L_0 b_0}\right| \tag{20}$$

2.7 Three-point Bending Testing

The deformation of the three-point specimen can be analysed as a beam-bending issue until cracks form [52]. The DIN EN ISO 178 [55] is used to conduct the bending test on polymers. The modulus of elasticity E_f is determined under bending stress conditions, using the same parameters as in tension and compression tests, i.e., as the secant modulus (Figure 12) in the range of 0.05 to 0.25 % strain of the outer fibre.

$$E_f = \frac{\sigma_{f2} - \sigma_{f1}}{\varepsilon_{f2} - \varepsilon_{f2}} = \frac{\Delta\sigma}{0{,}002} \tag{21}$$

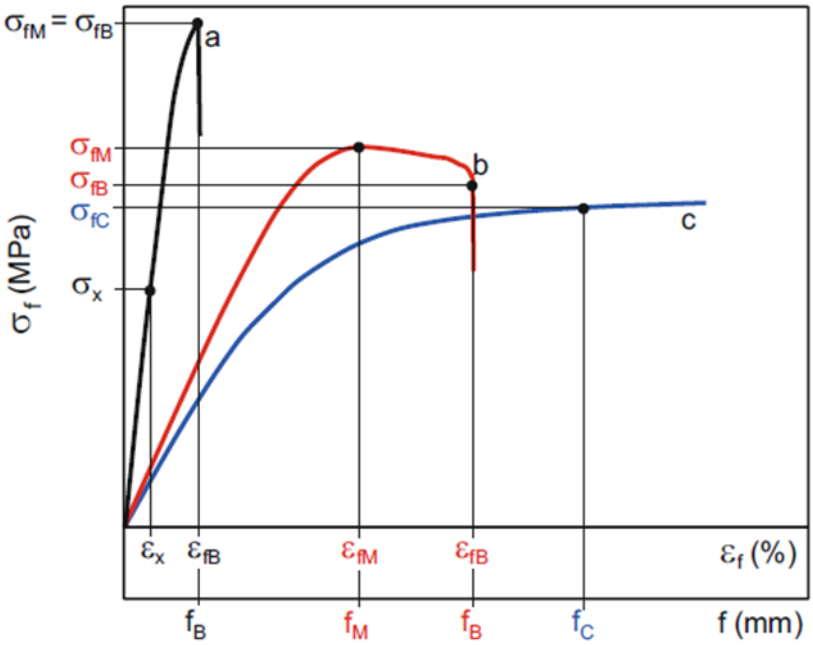

Figure 13: Characteristic bending stress-strain curves for polymers: a) brittle, ductile and elastic material behaviour [38].

Figure 13 displays typical bending stress-strain curves for various polymers. The diagram in Figure 13 (curve a) illustrates the behaviour of a material such as PS or PMMA, which is relatively brittle. For ductile material behaviour (curve b in Figure 13), a maximum force occurs and fracture happens before reaching the so-called standard deflection. In this case, flexural strength can be determined at maximum load. If the materials being examined do not exhibit a maximum force or fracture until reaching the standard deflection the norm bending stress σ_{fC} is determined (equation (22)) at this point, with this material behaviour also being ductile [6, 38]. Curve c in Figure 13 represents elastic material behaviour of polymers such as TPU. It allows us to establish the specific parameters for different polymers.

$$\sigma_{fC} = \frac{3F_C L}{2bh^2} \tag{22}$$

2.8 Viscosity

Polymer melts, which are viscoelastic fluids, hold significant technical significance. These substances possess intricate rheological properties that give rise to a multitude of diverse phenomena [35]. The classification of flow and viscosity curves can be achieved by considering the purely viscous and plastic viscosities of different substances based on specific criteria, as shown in Figure 14.

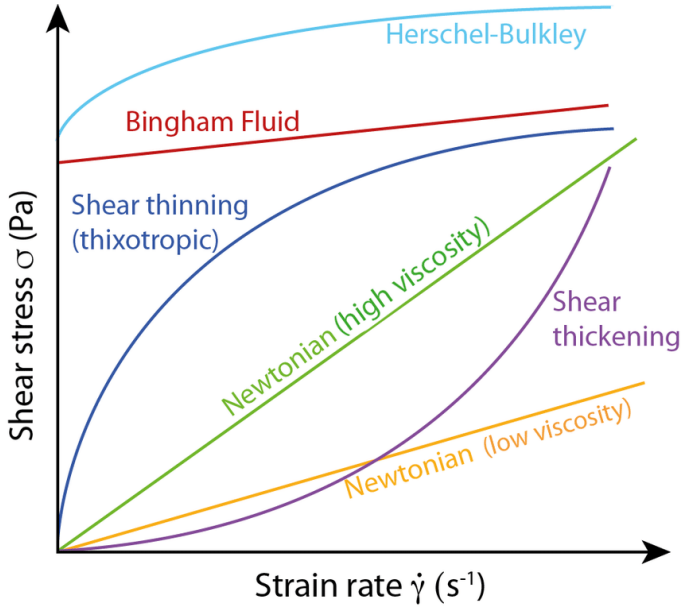

Figure 14: Characterization of viscous liquids in the flow diagram [50]

Viscosity curves are approximated using a range of function types, including empirical, semi-empirical, and theoretically based methods. There exist various shear stress methodologies that have the capability to characterise the viscosity curve comprehensively or partially (shown in Figure 15). The power-law is frequently employed due to its inherent mathematical simplicity and describes the structurally viscous and dilatant material behaviour [77]:

$$\tau = k\dot{\gamma}^n \tag{23}$$

τ denotes shear stress, n signifies the flow index, $\dot{\gamma}$ is the shear rate and k represents the consistency. The Sisko Model is employed to characterize high shear rates [65]:

$$\eta = \eta_\infty + \mathrm{k}\dot{\gamma}^{n-1} \tag{24}$$

with η_∞ as the infinite viscosity, k the consistency and n the power law index.

The three-parameter approach proposed by P.C. Carreau incorporates the quasi-Newtonian range as well [68]:

$$\tau = \frac{\eta_0 \dot{\gamma}}{\left(1 + \frac{\dot{\gamma}}{\dot{\gamma}_c}\right)^c} \tag{25}$$

where η_0 denotes the viscosity at low shear rates, c represents the absolute value of the asymptote gradient for high shear rates, and $\dot{\gamma}_c$ the location of the curved surface.

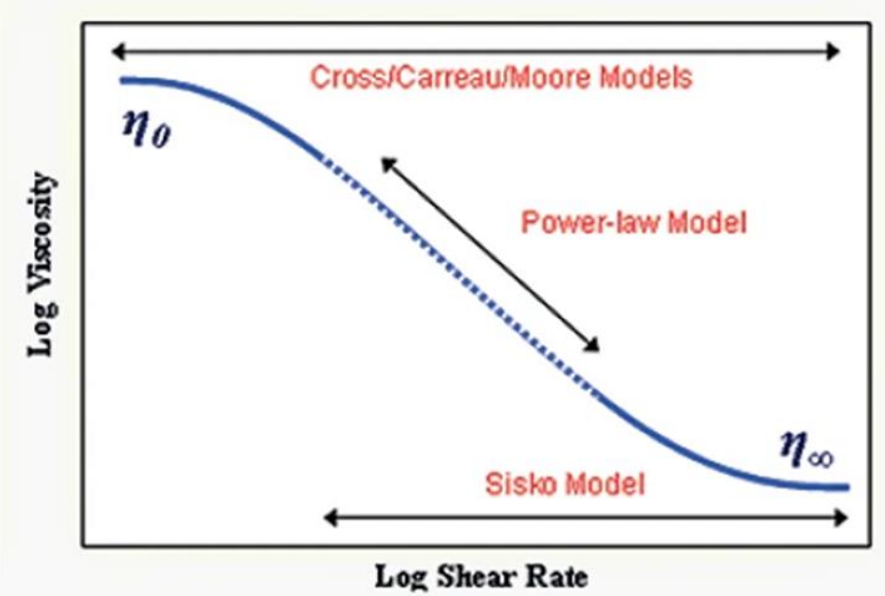

Figure 15: Area of application for different approach function to the viscosity curve [71].

Viscosity is also known to possess an exponential relationship with temperature, often described by the Arrhenius expression for Newtonian fluids and semi-crystalline polymers:

$$\eta = Be^{E/RT} \tag{26}$$

Where E represents the activation energy, R is the gas constant, and T stands for the absolute temperature. This equation is typically appropriate for explaining how viscosity changes with temperature, as long as the temperature range is not extensive. Analytical work can be rewritten in a more useful form [22, 92].

$$\eta = \eta_R exp\frac{E}{R}\left(\frac{1}{T} - \frac{1}{T_R}\right) \tag{27}$$

where T_R represents a convenient reference temperature and η_R is the viscosity at the reference temperature. At temperatures above the glass transition temperature, methods based on the Williams-Landel-Ferry (WLF) model have been widely accepted. This notion is utilised to define amorphous polymers and can be expressed in the following manner [64]:

$$log\left(\frac{\eta(T)}{\eta_{T_{ref}}}\right) = -\frac{C_1\left(T - T_{ref}\right)}{C_2 + \left(T - T_{ref}\right)} \tag{28}$$

The variable $\eta(T)$ represents the Newtonian or apparent viscosity at an absolute temperature T, while $\eta_{T_{ref}}$ represents the viscosity at an arbitrary absolute reference temperature T_{ref} and two variable parameters C_1 and C_2.

3 Redesign 3D-Printer

This chapter provides a comprehensive explanation of the procedure for reconstructing the HAGE 3Dp-A2 printer (shown in Figure 16). It involves the installation of two dual extruders that can be controlled separately, as well as a complete overhaul of its electronic components.

3.1 Original Components

The HAGE 3D printer (shown in Figure 16) is a Cartesian printer with a generous build volume of 620 x 400 x 290 mm^3, allowing for the installation of two dual extruders while still maintaining considerable printing space. The printing bed has a 1000 W heating element, which guarantees fast heating [82]. It is controlled by four independent stepper motors on the z-axis. In addition, the x-axis is also driven by two separate stepper motors. The original direct dual extruder, which is mounted to the y-axis, has been removed from the printer. A detailed and thorough description of the redesign will be presented in the following pages. In addition, all electrical components, including the power supply, were removed.

Figure 16: HAGE 3DpA-2 printer [82]

3.2 Y-axis Carriage

The printer's standard setup included a single stepper motor that controlled the y-axis. To enable the movement of two independent extruders, an additional stepper motor had to be installed. Figure 17 displays the extruder carriages attached to the main mounting plate for the extruders, which can be mounted on the front side using the mounting holes. The rear part of the component features a mechanism for adjusting the tension of the belt and a bracket designed to hold linear ball bearings. The second extruder carriage includes an extra mounting spot for an adjustable screw, which will be detailed in section 3.3.

The drill holes are all 3 mm in diameter to accommodate M2.5 metal threads. This approach renders the utilisation of nuts unnecessary and eliminates the need for any additional geometries specifically designed for nuts. The carriage's dimensions are 105 x 50 x 29.5 mm^3 and 105 x 50 x 37.5 mm^3, respectively.

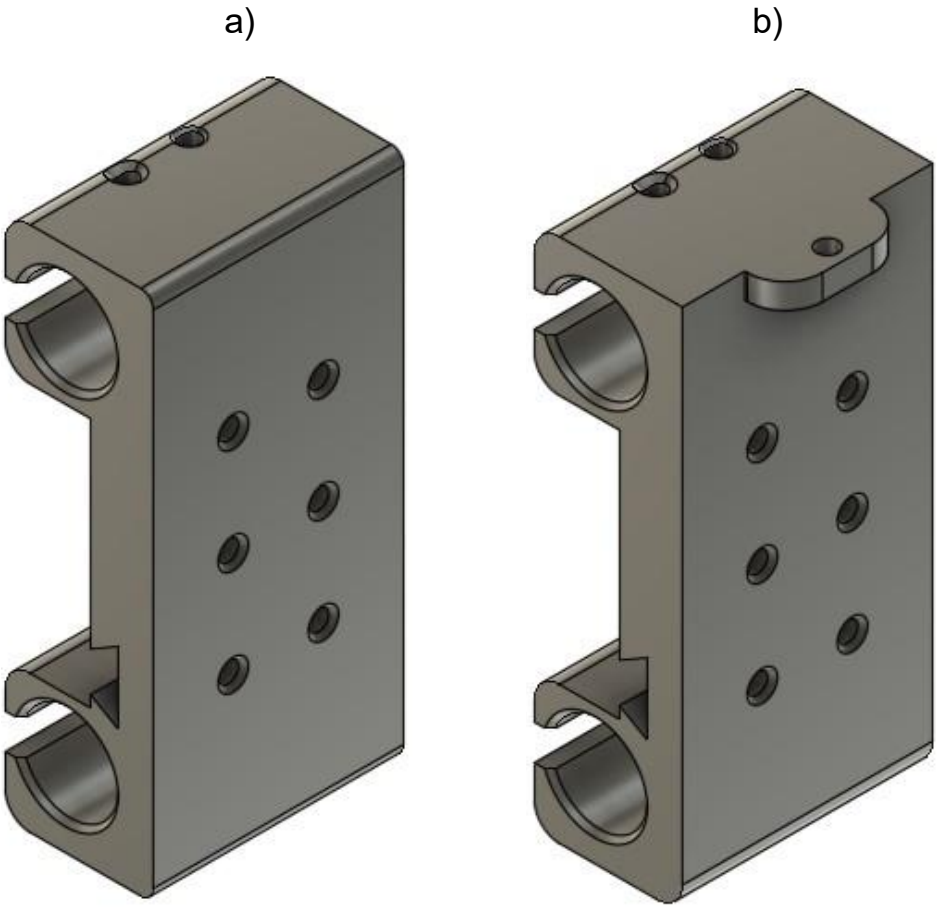

Figure 17: a) Extruder carriage for the primary extruder mount, b) extruder carriage for the secondary extruder mount.

3.3 Dual Extruder Mount

Figure 18 illustrates the mounting system for both dual extruders. The direct extruder is positioned on the right side of the mounting plate, while an adjustable bowden extruder is located on the left side (shown in Figure 19). Both designs feature a cylindrical shape that fits a standard E3D heat sink to secure the extruders in place. The slot holes allow manual

adjustment of the nozzle's position relative to the reference point. The recess on the back of the component ensures that the extruder is cantered and guided longitudinally. The rationale behind this particular configuration is twofold: firstly, to minimize weight by utilizing only a single direct extruder, and secondly, to facilitate cable management due to insufficient space within the current drag chains. The main mounting plate also includes a holder for the BL-Touch.

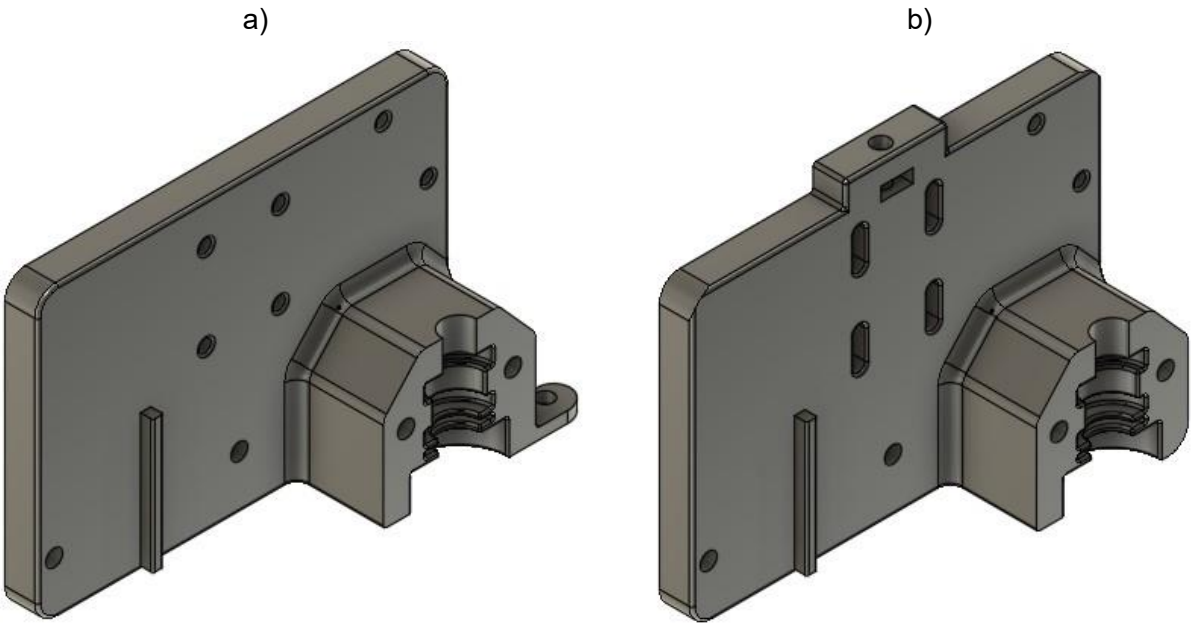

Figure 18: a) primary mounting plate for extruders, b) secondary mounting plate for extruders

The nozzle on the direct extruder of the primary mounting plate functions as a point of reference for adjusting the other nozzles. The bowden extruders can be manually adjusted using an adjustable bowden mount. To enable adjustments to the direct extruder, the secondary mounting plate must possess the capability of movement. Therefore, a screw, along with a spring, is installed on the upper side of the plate. Rotating the screw in a clockwise direction will cause the plate to rise, whereas rotating the screw in an anticlockwise direction will cause the plate to descend.

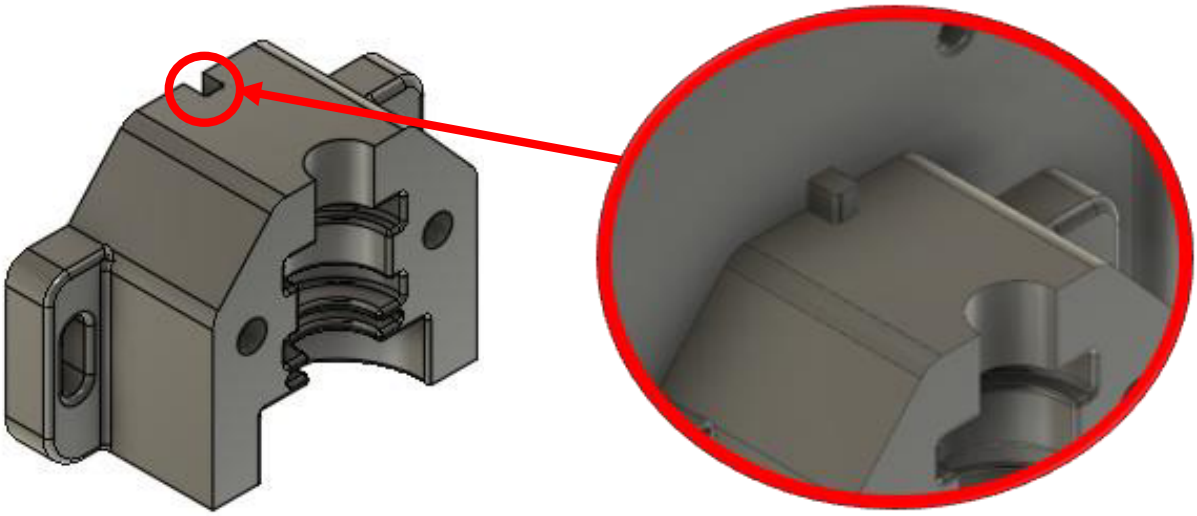

Figure 19: Bowden extruder mount.

The picture provided in Figure 20 depicts the complete configuration of the Quadro-extruder setup, including the mounting system for its cooling fans.

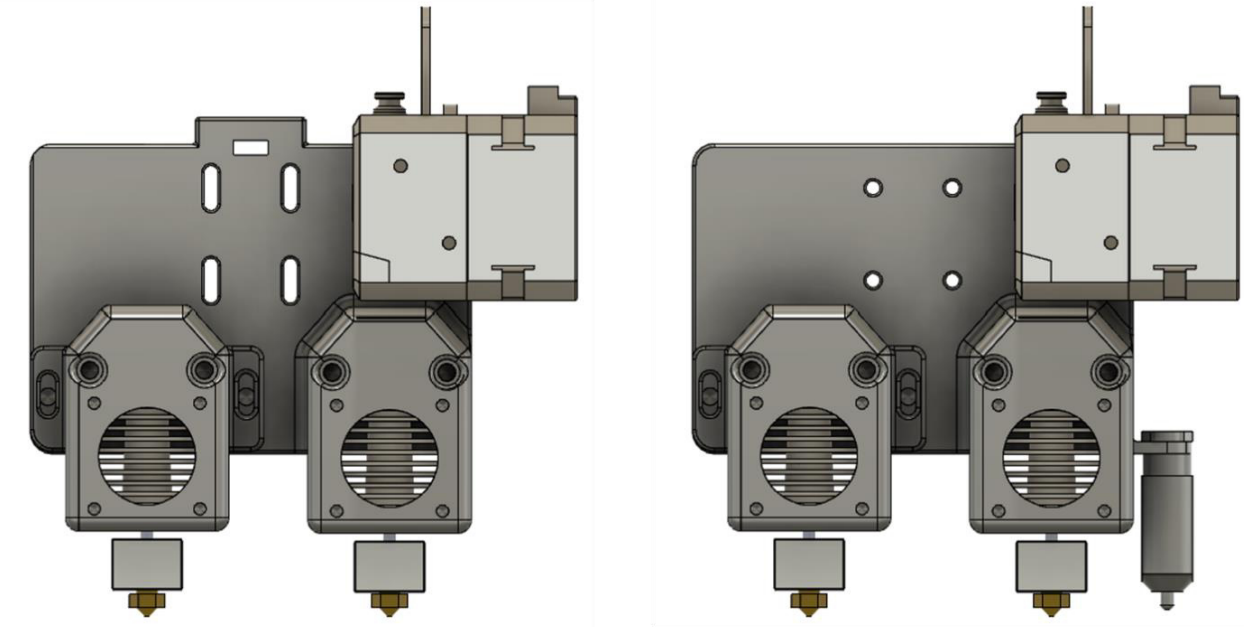

Figure 20: Fully assembled Quadro-extruder configuration, left secondary and right primary assembly.

3.4 Hardware

Extruder

The Bondtech LGX [14] was installed as the direct extruder, while the Bondtech LGX Lite [15] was used as the bowden extruder. Their use of dual-drive technology (both gears are driven, in contrast to many other constructions where only one is driven), which relies on large drive gears, offers an ideal choice for feeding extremely flexible filaments. The LGX extruders are compatible with full metal hotends and can be utilized as either a shortcut cooling solution or with standard heatsinks, which have been installed in this printer.

Mainboard and Power Supply

The primary criteria for the mainboard were a high-performance processor (minimum 32-bit chip) and the capability to support a minimum of eight stepper motors (the z-axis is operated separately). This involves managing four extruders, two for each y-axis, and two for the x-axis. The BIGTREETECH Octupus [98] was selected as it is one of the most powerful mainboards available in the commercial sector for 3D printers and has the capability to support up to 8 stepper motors. The previous system operated at a voltage of 12 volts. To achieve an industrial standard of 24 volts, the motherboard needed to have the capability to support this voltage level.

The chosen power supply, with a 500 W output, was essential due to the simultaneous heating of all extruders, resulting in a power consumption of 2000 Watts.

Arduino and CNC Shield

The HAGE printer features a large printing bed that is mounted on four threaded rods and driven by four stepper motors. To achieve precise calibration, it is crucial to individually control each motor for accurate adjustments. Thus, it is necessary to install an additional micro control unit that possesses adequate processing capabilities. The Arduino Mega [5] was used in combination with a CNC shield [47] in this specific setup. The device functions as a control module for a 3D printer, equipped with four connections made for stepper motors.

BL-Touch

The printer was equipped with an Antclabs [4] levelling sensor to guarantee the consistent thickness of the first layer. The sensor scans a specific quantity of measuring points on the printing bed and calculates the precise height at which the sensor makes contact. The measuring points are utilized to elongate a simulated mesh and automatically correct the difference in height during the printing process.

3.5 Firmware

The printer utilized Klipper as its designated firmware. The software was installed on a Linux Ubuntu server, which is responsible for linking most of the printers in the facility. Uploading new software and transferring data directly to the Klipper directory eliminates the need for SD cards to flash the motherboard, providing a convenient solution for making swift changes to the firmware. Through the use of Python code, the process of incorporating customized codes into the firmware is made more straightforward. Furthermore, it allows for the generation of macros that can be called via the Slicer software. Mainsail OS was selected as the user interface for Klipper. It is a web interface that enables the control and management of 3D printers.

Figure 21 displays the key attributes of the interface. The left-side panel contains various available settings. The main feature is the dashboard, which exhibits the real-time status of the printer while a print job is in progress. A control panel for managing all axes, including the control of filament extrusion and retraction. The current extruder's z offset and a list of available macros that can be used. The centre of the display shows the telemetry of the extruder and bed temperature, along with a real-time graph. The console, located on the right side, displays the G-code steps or the output of specific data points.

The "G-Code file" displays all the uploaded print files that can be directly modified in the web interface. All crucial printer configurations are stored in the "machine". The "machine" settings contain, for each attached MEX printer, the pin assignment of the circuit board, the dimensions of the printing bed, as well as customized macros.

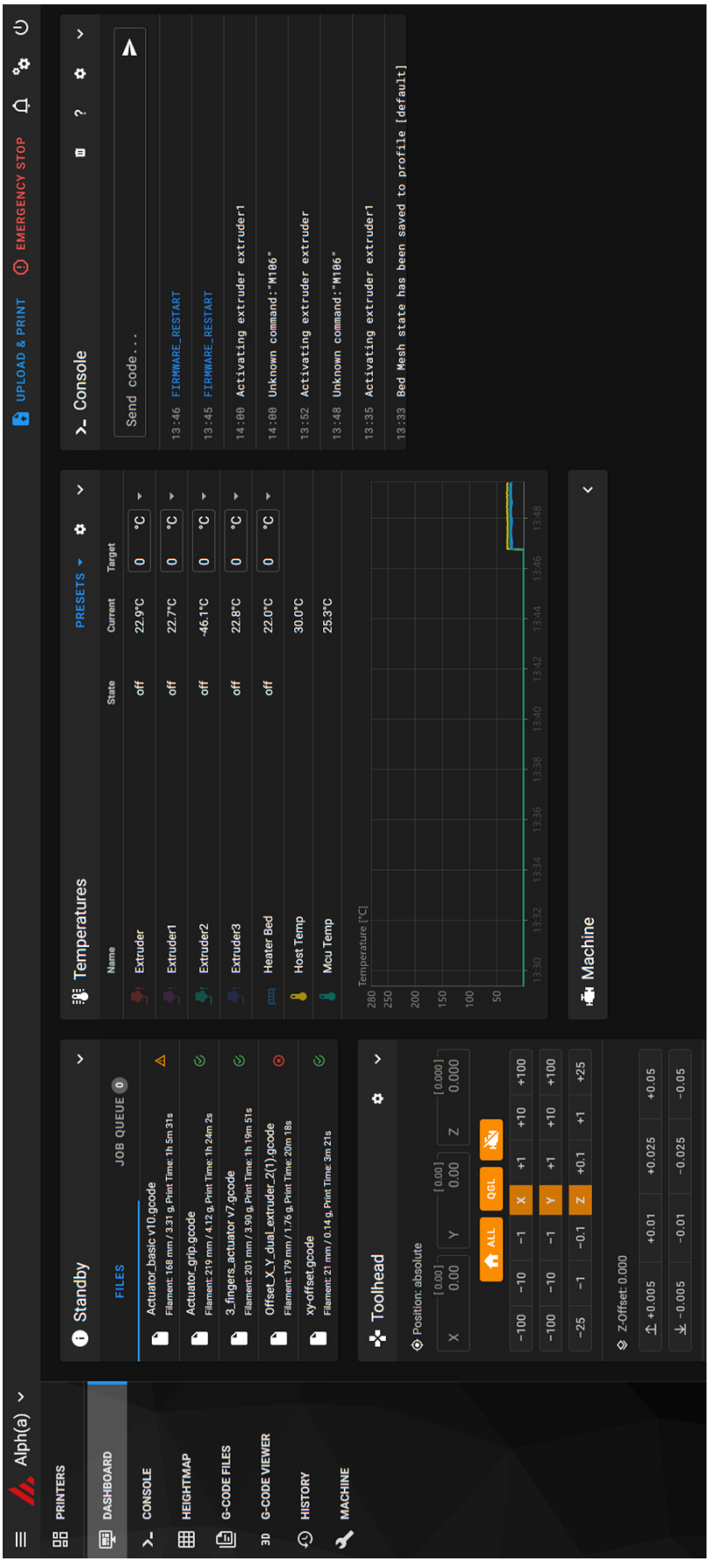

Figure 21: Web user interface.

3.6 Calibration and Macros

The calibration of each nozzle is an essential component for ensuring the precision of the printer. As stated in 3.3, the initial step involves manually adjusting the nozzle height relative to the reference point, which is the primary extruder mount with the direct extruder's nozzle.

The precise location of the reference point is determined by the distance of the levelling sensor, as depicted in Figure 22. The direct extruder and bowden extruder are separated by 55 mm.

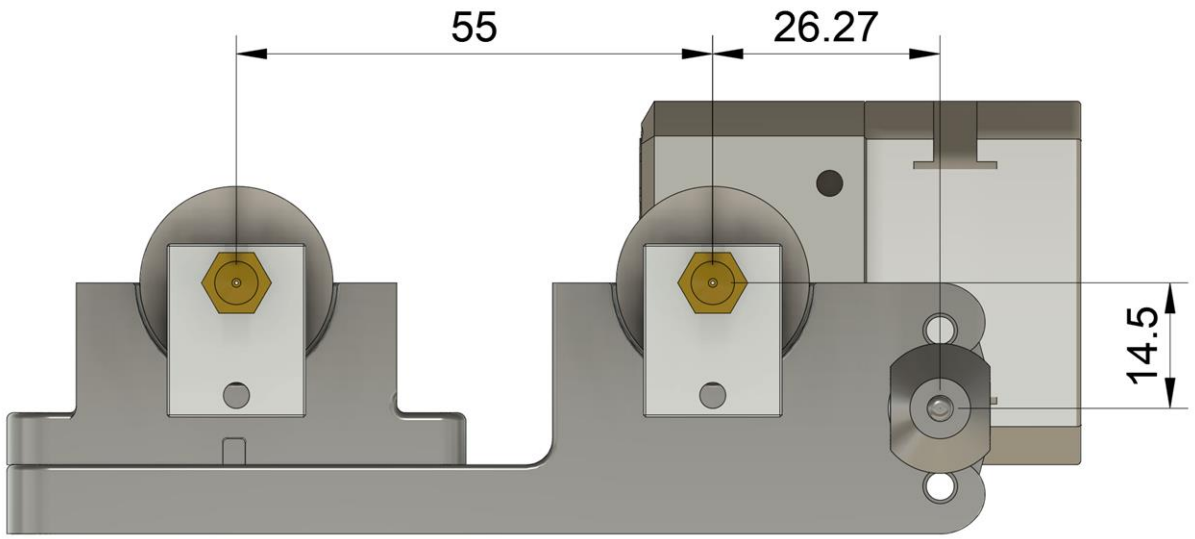

Figure 22: Distance from bowden extruder to direct extruder and from direct extruder to BL-Touch.

The distance between the primary extruder mount and the secondary extruder mount was adjusted using two mechanical endstops on the y-axis. The distance d_{sse} is 550 mm, determined by adding the distance between the endstops l_{a+} to the distance between the endstop and the direct extruder position d_{ssee}.

$$d_{sse} = l_{a+} d_{ssee} \tag{29}$$

“Tool change” Macro

To ensure smooth tool changes during the printing process, it was necessary to develop and integrate specific macros into the slicer software. The macro takes into account both a G-code offset and a bedmesh offset, ensuring accurate adjustments during the print (Figure 23).

The G-code offset allows for fine tuning of the nozzle distances. The value of the nozzle depends on its position. If the nozzle lies on the negative axis, the value is positive. Conversely, if the nozzle is on the positive axis, the value is negative.

“Nozzle clean” Macro

Following tool changes, the extruder that is not in use is cooled down to a temperature approximately 50 K lower than the processing temperature. This is done to prevent the material from leaking out of the nozzle, a phenomenon known as oozing.

Upon reactivating the extruder, it is possible for the material to retreat back into the nozzle as a result of the cooling process. To address this issue, a macro was devised to initially extrude a few millimetres and subsequently cleanse it using a mounted brush positioned at the forefront of the printing bed before recommencing the printing process.

```
# Activate the primary extruder
[gcode_macro T0]
gcode:
    {% if printer.toolhead.extruder.can_extrude%}
    {% endif %}
    {% if printer.toolhead.extruder == "extruder1" or printer.toolhead.extruder == "extruder3"%}
        PARK_extruder1
    {% endif %}
    BED_MESH_OFFSET X=0 Y=0
    SET_GCODE_OFFSET X=0 Y=0 Z=0
    ACTIVATE_EXTRUDER EXTRUDER=extruder
    SET_DUAL_CARRIAGE CARRIAGE=0
    {% if printer.toolhead.extruder.can_extrude%}
    {% endif %}
```

Figure 23: Offset settings for extruders threw macro.

This procedure will be executed each time a tool change takes place. It will substantially prolong the printing duration but guarantee better quality for the printed component.

```
[gcode_macro CLEAN_NOZZLE]
gcode:
 SAVE_GCODE_STATE NAME=clean
 {% if printer.toolhead.extruder == "extruder" or printer.toolhead.extruder == "extruder2" %}
   _CLEAN_NOZZLE1
 {% else %}
   _CLEAN_NOZZLE2
 {% endif %}
 RESTORE_GCODE_STATE NAME=clean

[gcode_macro _CLEAN_NOZZLE1]
variable_start_x: -12
variable_start_y: 90
variable_start_z: 27.5
variable_wipe_dist: 60
variable_wipe_qty: 3
variable_wipe_spd: 50
variable_raise_distance: 30
variable_purge: 15

gcode:
 {% if "xyz" not in printer.toolhead.homed_axes %}
   G28
 {% endif %}


 G90
 ## Purge position
 G1 Z{start_z} F1500
 G1 X{start_x} Y{start_y-10} F6000
 M83
 G1 E{purge} F60
 ## Move nozzle to start position
 G1 Z{start_z} F1500
 G1 X{start_x} Y{start_y} F6000


 ## Wipe nozzle
 {% for wipes in range(1, (wipe_qty + 1)) %}
   G1 Y{start_y + wipe_dist} F{wipe_spd * 60}
   G1 Y{start_y} F{wipe_spd * 60}
 {% endfor %}
 G1 X50

```

Figure 24: Nozzle clean macro for tool change.

4 Experimental

This section concentrates on analysing materials for the actuators passive layer by producing specimens for tensile tests and three-point bending tests using different infill orientations.

Viscosity measurements were conducted for the dielectric component of the actuator, and the dielectric constant was determined. In the next step, multi-material actuators were manufactured, and their capacitance and maximum displacement were determined.

4.1 Materials

Various thermoplastic polyurethanes with different shore hardness levels were utilised. Table 1 presents the chosen materials for the electrodes along with their key properties.

Table 1: Electrode filaments with specified data sheet information.

Filament	**Electrical resistivity**	**Hardness**
Eel™ TPU 3D [73] (Fenner Inc., USA)	1500 Ω/cm^2 (ANSI/ESD STM 11.11)	Shore A 90
CONDUCTIVE FILAFLEX TPU [83] (RECREUS INDUSTRIES S.L., SPAIN)	< 60 Ω (ASTM D 257)	Shore A 92

Table 2 displays the materials used as the dielectric component for the actuators, whereas Table 3 lists the materials used as the passive layer of the actuator.

Table 2: Dielectric components of the actuator and experimentally determined dielectric constant.

Filament	**Dielectric constant**	**Hardness**
NinjaFlex® EDGE [75] TPU (Fenner Inc., USA)	3.65	Shore A 83
NinjaFlex® TPU [74] (Fenner Inc., USA)	4.96	Shore A 85

Table 3: Filaments used as passive components.

Filament	**Hardness**
NinjaFlex® TPU (Fenner Inc., USA)	Shore A 85
Cheetah® [72] TPU (Fenner Inc., USA)	Shore A 92
Fiberlex 20D [33] (Fiberlab S.A., PL)	Shore D 20
Fiberlex 40D [34] (Fiberlab S.A., PL)	Shore D 40

4.2 Printing Parameters

Each material's process temperature ranges from 220 °C to 250 °C, while the bed temperature can be raised to 50 °C or turned off. Every test specimen was printed using identical configurations on the Prusa Mk3S+(Prusa, CZ). The printer configurations were implemented as per the initial suggestions provided by the Prusa Slicer software. The utilized infill pattern consisted of a linear rectangle, which was applied to produce specimens with infill orientations of 0° and 90°, respectively. In the slicer program, the sequential print option was used to print five test specimens for each orientation.

Table 4 lists the most important parameters of the print and filament settings.

Table 4: Print settings for test specimens.

Print settings	**Value**	**Unit**
Layer height	0.1	mm
Perimeter	1	-
Infill	100	%
Infill pattern	linear Rectangle	-
Printing speed	20	mm/s
Nozzle temperature	240	°C
Bed temperature	Off	-
Printer parameters		
Build platform	Satin Powder-coated Steel Sheet	

4.3 Tensile Test and Three-point Bending Test

At the Institute of Materials Science and Testing of Polymers, the experiments were carried out using a universal testing machine manufactured by Zwick Roell GmbH & Co. KG (Germany) for the tensile tests and the three-point bending test.

The test specimen's geometry dimensions for the tensile test were chosen in accordance with the standard ISO 527-2-5A [27] (Figure 25). This geometry was selected to optimize material conservation, considering the availability of certain filaments.

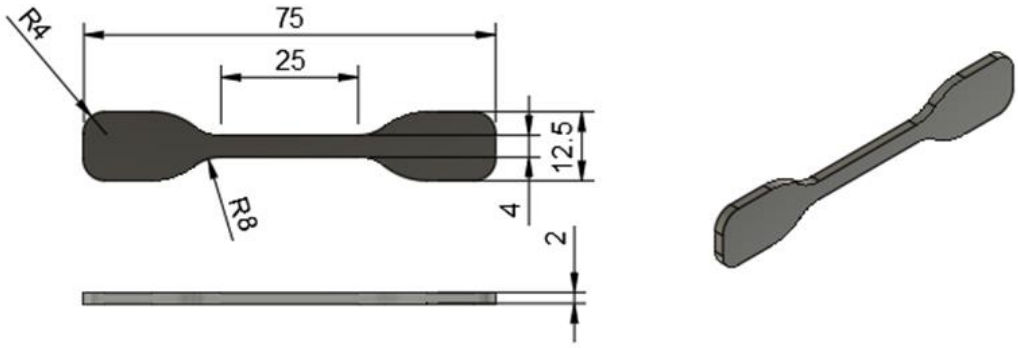

Figure 25: Geometry of tensile test specimen according to ISO 527-2-5A.

Figure 26 displays the dimensions of the specimen used in the three-point bending test as per the ISO 178.

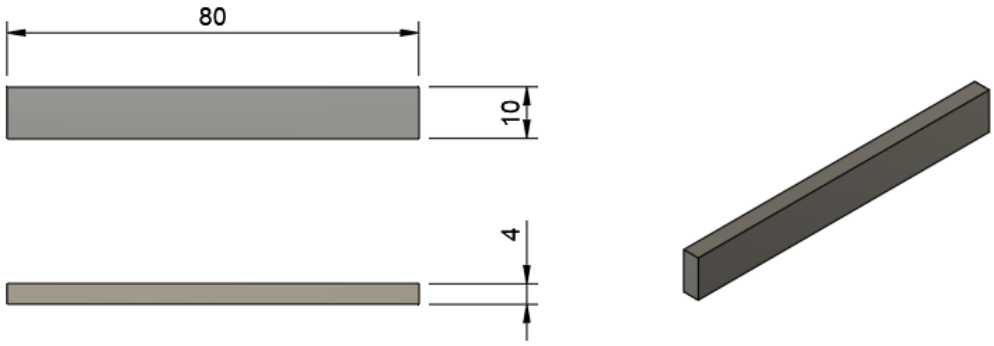

Figure 26: Geometry of tensile test specimen according to ISO 178.

4.4 Permittivity Measurement

The measurement configuration (Figure 27) remained in a fairly uncomplicated manner. The relative dielectric constant of the membrane material was determined by employing a cooper sheet as the bottom electrode and a steel cylinder as the top electrode. The membrane was placed between the two materials, and the capacitance was measured using a multimeter manufactured by Conrad Electronic AG (Switzerland). By rearranging equation (4), the permittivity of the material can be obtained. In Table 5, the relevant dimensions of the measurement are presented.

Table 5: Measurement setup with essential dimensions.

Index	**Element**	**Area**	**Thickness**
a	Cooper sheet	100 x 100 mm^2	1 mm
b	Dielectric membrane	$625 \cdot \pi$ mm^2	0.3 mm
c	Steel cylinder	$225 \cdot \pi$ mm^2	25 mm

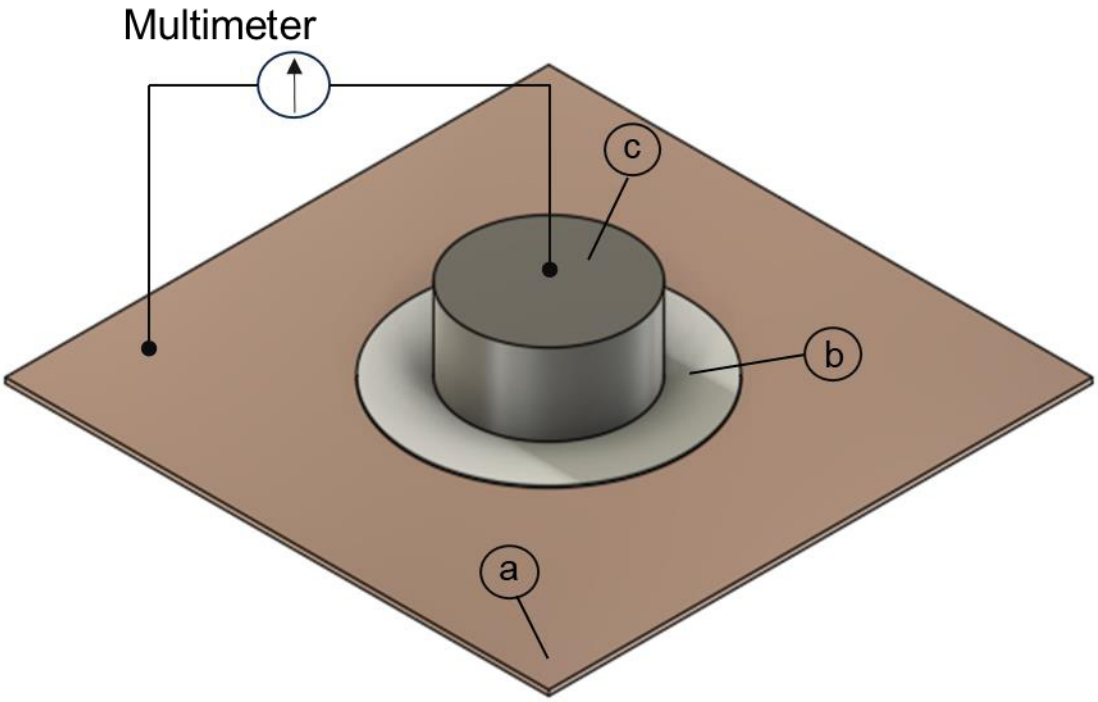

Figure 27: Measurement setup for the relative dielectric constant: a) cooper sheet, b) dielectric membrane and c) steel cylinder.

4.5 Viscosity Tests

The measurement of viscosity was performed using the High-Pressure Capillary Rheometer (HPCR) Rheograph 2002, manufactured by Göttfert Werkstoff-Prüfmaschinen GmbH in Germany. In order to replicate authentic pressure conditions to the maximum extent feasible, a custom-designed adapter for a nozzle attachment was employed (Figure 28). In addition, it is necessary to convert the volumetric speed $\dot{V}$ obtained from the printing process, into the piston speed v_P using the following equation:

$$v_P = \frac{\dot{V}}{A} \tag{30}$$

where A is the area of the piston.

Three measurements were conducted for each material, with one cylinder filled and 20 measuring points. Table 6 contains the test parameters for the viscosity measurements.

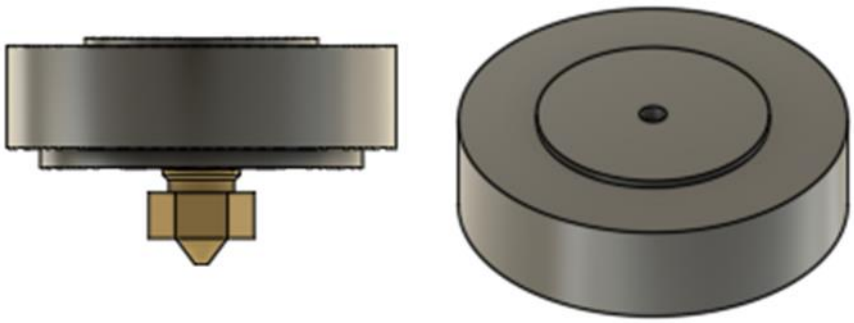

Figure 28: Adapter with E3D nozzle.

Table 6: Parameters for the viscosity measurement.

Parameters	**Value**	**Unit**
Volumetric speed	1.5	mm^3/s
Shear rate	239.4	1/s
Piston speed	0.01735	mm/s
Temperature	190	°C
Diameter of the capillary	0.4	mm
Length of the capillary	0.6	mm

4.6 Actuator

4.6.1 Geometry

Figure 29 depicts the design of a soft multi-material actuator. The structure includes a passive layer made of materials specified in Table 3, two electrically conductive materials identified in Table 1 that act as electrodes, and a dielectric membrane from Table 2.

Table 7 displays the dimensions of each layer of the actuator.

Table 7: Layer structure and dimensions of the actuator.

Index	**Layer**	**Length in mm**	**Width in mm**	**Height in mm**
a)	Passive	90	45	0.1
b)	Electrode	66	37	0.07
c)	Dielectric membrane	90	45	0.21
d)	Electrode	66	37	0.07

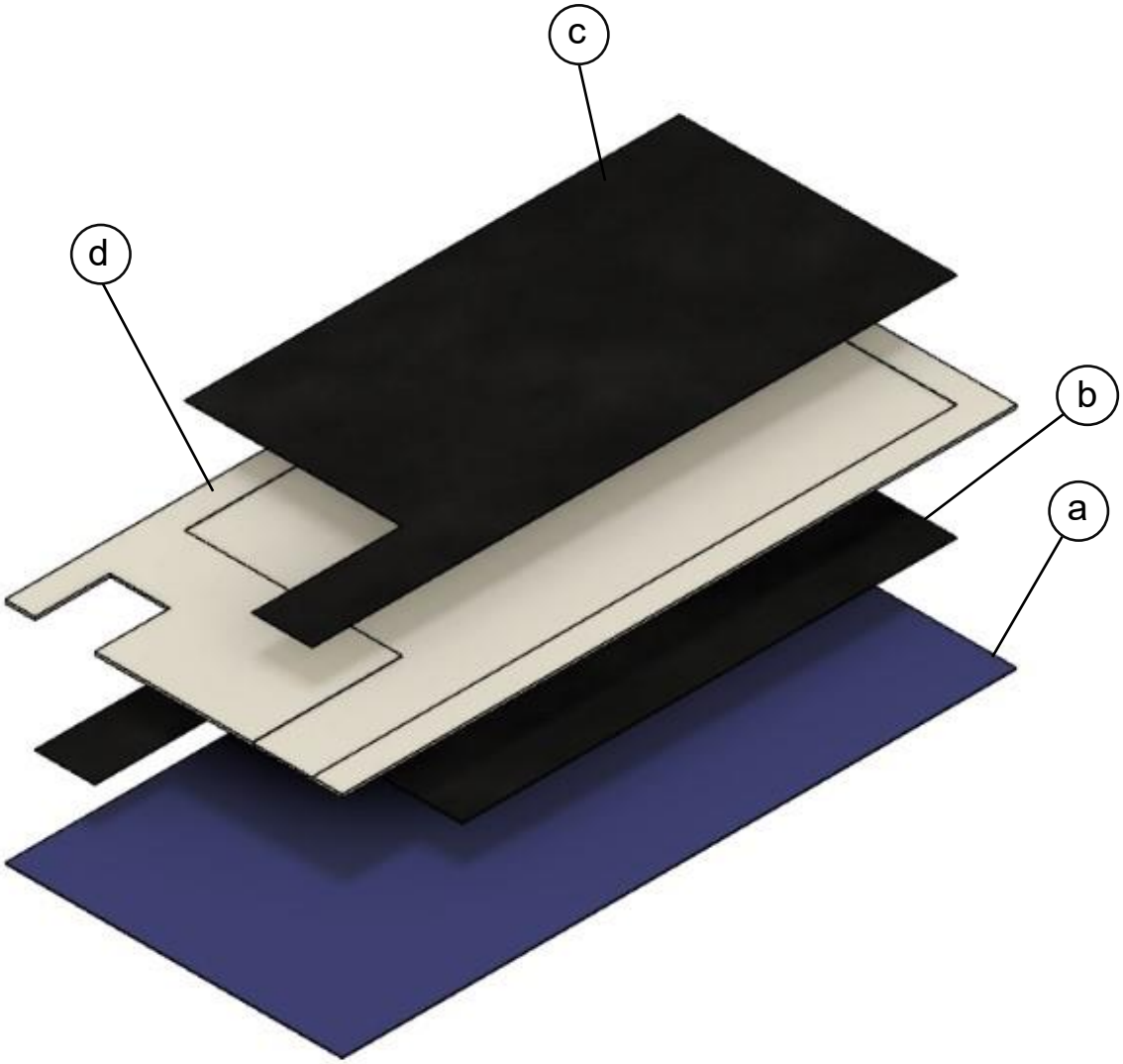

Figure 29: Design of the multi-material Actuator: a) passive layer, b) electrode c) dielectric membrane and d) electrode.

4.6.2 Printing parameters

A total of 3 actuators were printed for each combination of materials as a result of the limitations caused by the available materials. The print parameters and specific filament settings for each material are presented in Table 8.

Table 8: Print settings for the actuators.

Print settings	**Value**	**Unit**
First layer height	0.1	mm
Layer height	0.07	mm
Perimeter	1	-
Infill	100	%
Infill pattern	Rectangle	-
Printing speed	10	mm/s
Nozzle temperature	240	°C
Bed temperature	Off	-
Retraction (direct extruder)	6	mm
Retraction (Bowden extruder)	15	mm
Printer parameters		
Build platform	Glass	

Table 9 displays the various combinations of the printed actuators and their corresponding nomenclature.

Table 9: Combinations of printed actuators.

Name	**Passive Layer**	**Electrode**	**Dielectric membrane**
20DFILA	FiberFlex20D	FilaFlex	NinjaFlex
40DFILA	FiierFlex40D		
CheFILA	Cheetah		
NinjaFILA	NinjaFlex		
20DEEL	FiberFlex20D	Eel	
40DEEL	FiberFlex40D		
CheEEL	Cheetah		
NinjaEEL	NinjaFlex		

5 Results

The following section provides an account of the outcomes of the material tests and the functionality of the actuators.

5.1 Tensile Test

Figure 30 depicts a demonstration of the tensile test results performed on each material. The observed trend suggests that there is nearly no disparity in the modulus between the 0° and 90° orientations. This phenomenon is seen in almost all materials that were subjected to testing.

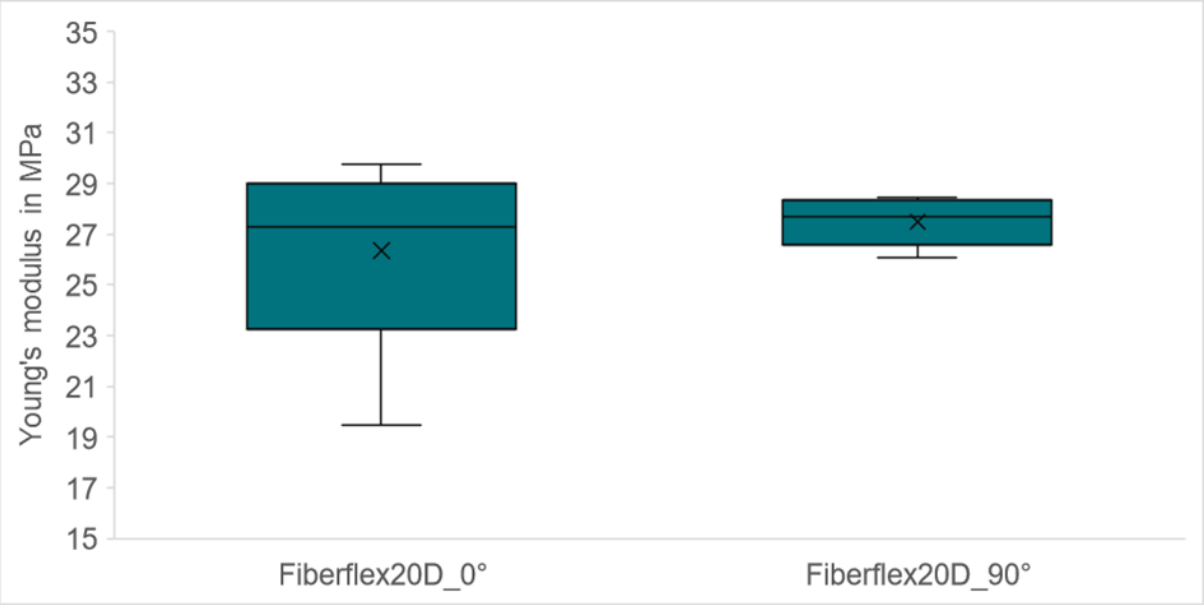

Figure 30: Young moduli for FiberFlex20D with orientations of 0° and 90°.

Figure 31 presents a comprehensive summary of the results obtained from all tests. Moreover, the diagram classifies the materials based on their functionality within the actuator. The findings indicate that there is no significant disparity in the orientations of 0° and 90°, except for FilaFlex_0° and FilaFlex_90°. FiberFlex40D exhibits a notable fluctuation in data dispersion. One potential cause for this could be attributed to quality deficiencies during the printing process. According to the data, both the electrode materials and Fiberflex 40D exhibit the highest modulus values. Nevertheless, it is not possible to definitively establish a direct relationship between hardness and the Young's modulus. This is exemplified by the fact that the highest values were achieved by a seemingly less rigid material. Table 10 presents a comprehensive compilation of the outcomes derived from the tensile test.

Table 10: Mean value and standard deviation of the Young's modulus for the tested materials.

	Orientation	Mean value in MPa	Standard deviation in MPa
FiberFlex20D	0°	26.4	3.6
	90°	27.5	0.9
FiberFlex40D	0°	65.0	9.3
	90°	64.9	2.4
NinjaFlex_CHEETAH	0°	28.8	0.4
	90°	26.9	1.9
NinjaFlex	0°	30.8	1.6
	90°	28.7	0.7
FilaFlex	0°	84.1	1.6
	90°	73.9	1.7
NinjaFlex_EEL	0°	90.8	0.9
	90°	91.2	1.1

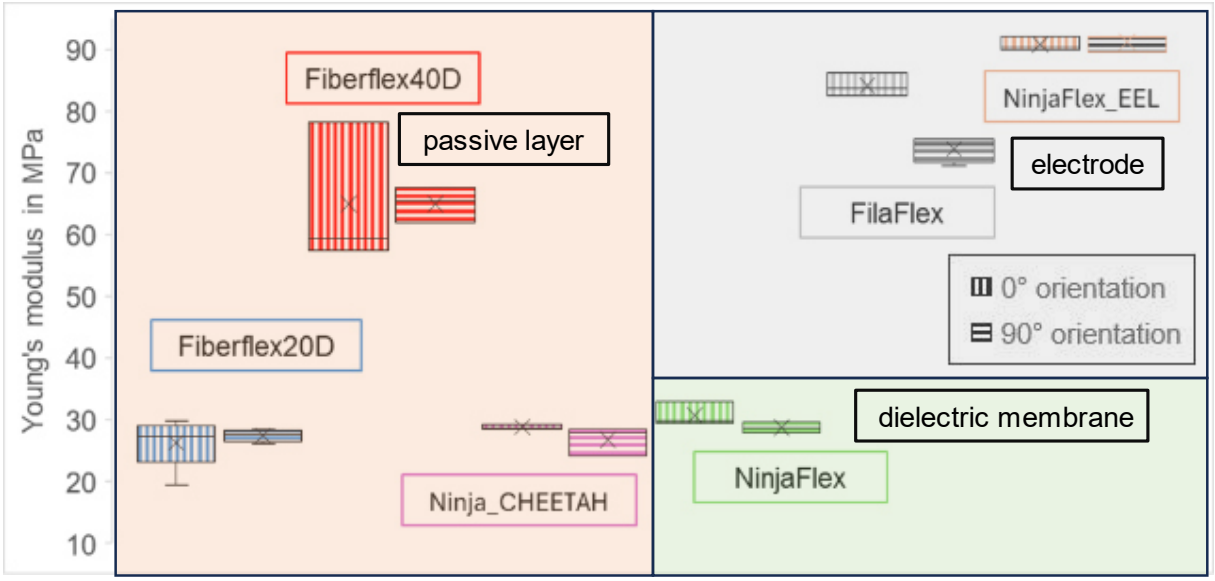

Figure 31: An overview of the tensile tests and categorized by their respective functionalities in the actuator.

5.2 Three-point Bending Test

In order to obtain additional information, the flexural modulus was determined, as the load case of the actuator primarily involves bending stress. It should be noted that this particular test is atypical for soft materials, specifically elastomers. However, the test results consistently align with the pattern described in chapter 5.1. Figure 32 illustrates the outcome.

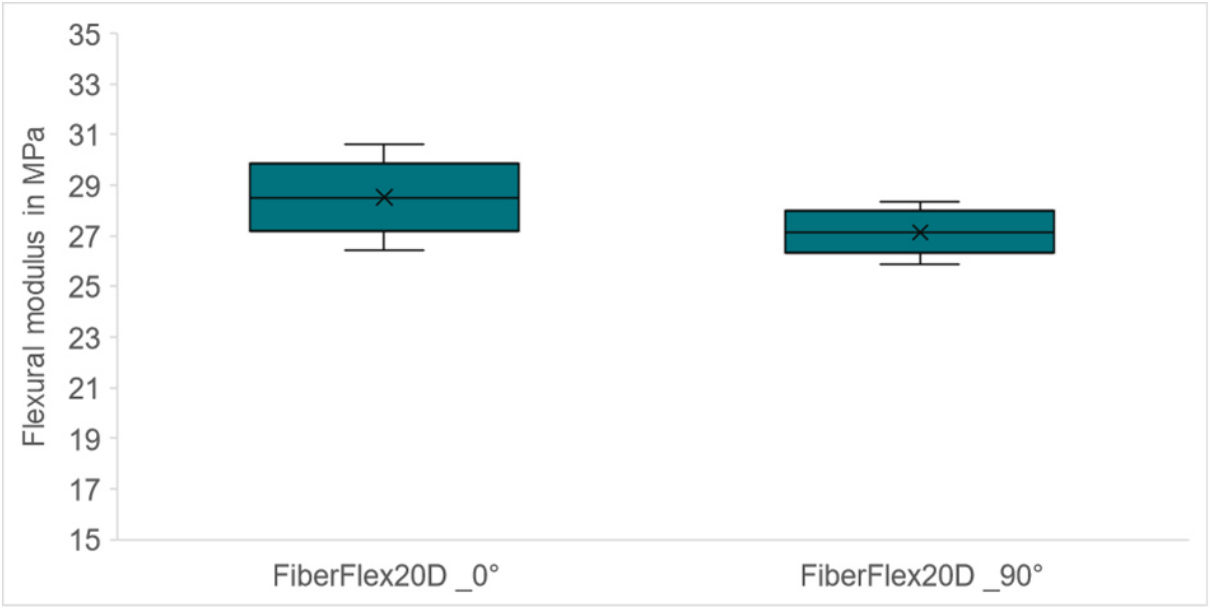

Figure 32:Flexural moduli for FiberFlex20D with orientations of 0° and 90 °.

An overview of the result is visible in Figure 33. This further illustrates that the stiffness of a material does not always correspond to its level of hardness. The results of the three-point bending tests confirm that FilaFlex_0° exhibits a significantly greater value than FilaFlex_90°. This this phenomenon may be attributed to the increased processing temperature, which leads to the melting and subsequent fusion of the individual strands, resulting in the loss of their original alignment.

Table 11: Mean value and standard deviation of the flexural modulus for the tested materials.

	Orientation	**Mean value in MPa**	**Standard deviation in MPa**
FiberFlex20D	0°	28.5	1.4
	90°	27.1	0.8
FiberFlex40D	0°	65.0	0.9
	90°	61.1	1.7
NinjaFlex_CHEETAH	0°	25.8	1.4
	90°	25.2	1.7
NinjaFlex	0°	26.7	0.5
	90°	26.2	0.9
FilaFlex	0°	79.6	1.1
	90°	65.3	3.4
NinjaFlex_EEL	0°	90.5	0.8
	90°	81.5	1.7

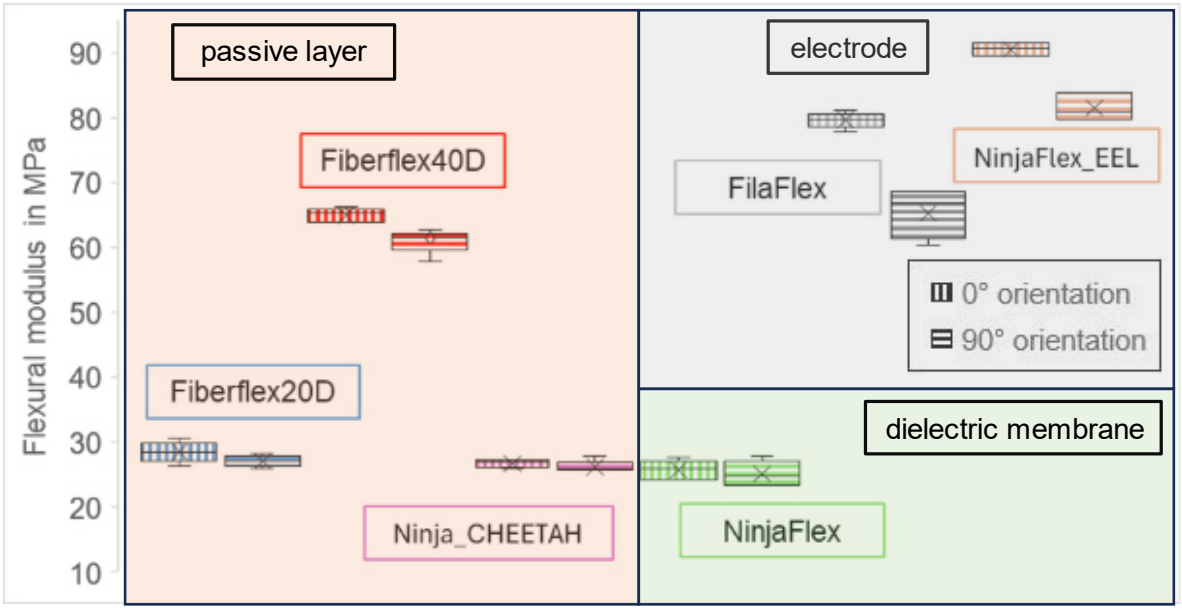

Figure 33: An overview of the three-point bending tests and categorized by their respective functionalities in the actuator.

5.3 Poisson's Ratio

The measured Poisson's ratio is not affected by the orientations. Furthermore, all materials possess similar values, except for NinjaFlex_EEL_0°, which clearly falls below the other results. The wide range of values limits the ability to make a conclusive statement. Both the process of preparing for a measurement and the actual measurement itself can be influenced by numerous potential sources of error. The primary issue with sample preparation comes to achieving a uniform coating on the specimen. Both the camera and programme must accurately identify and monitor the pigmentation in order to calculate the change in cross-sectional area with precision.

To obtain a precise depiction of Poisson's ratio, it is necessary to test a greater number of specimens. However, the range of values, specifically ranging from 0.36 to 0.4, for TPU's aligns with those reported in the literature [53].

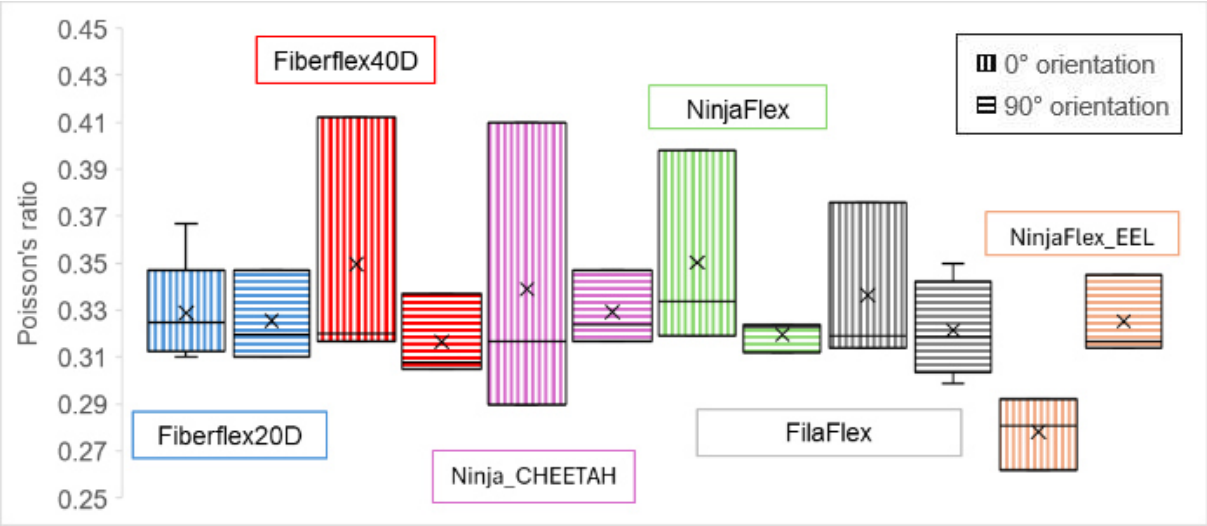

Figure 34: Poisson's ratio for all materials in 0° and 90° orientation.

5.4 Permittivity

During the study, Ninjatek introduced a new filament called NinjaFlex Edge to the market. The proclaimed shore hardness is measured to be 83A, indicating a slightly lower hardness compared to the Ninjetex 85A used in the conducted experiments. The initial results demonstrated superior printability compared to the material with a shore hardness 85A. The permittivity, however, exhibited a notable decrease, as depicted in Figure 35. This renders it unsuitable to serve as the membrane material for the actuators.

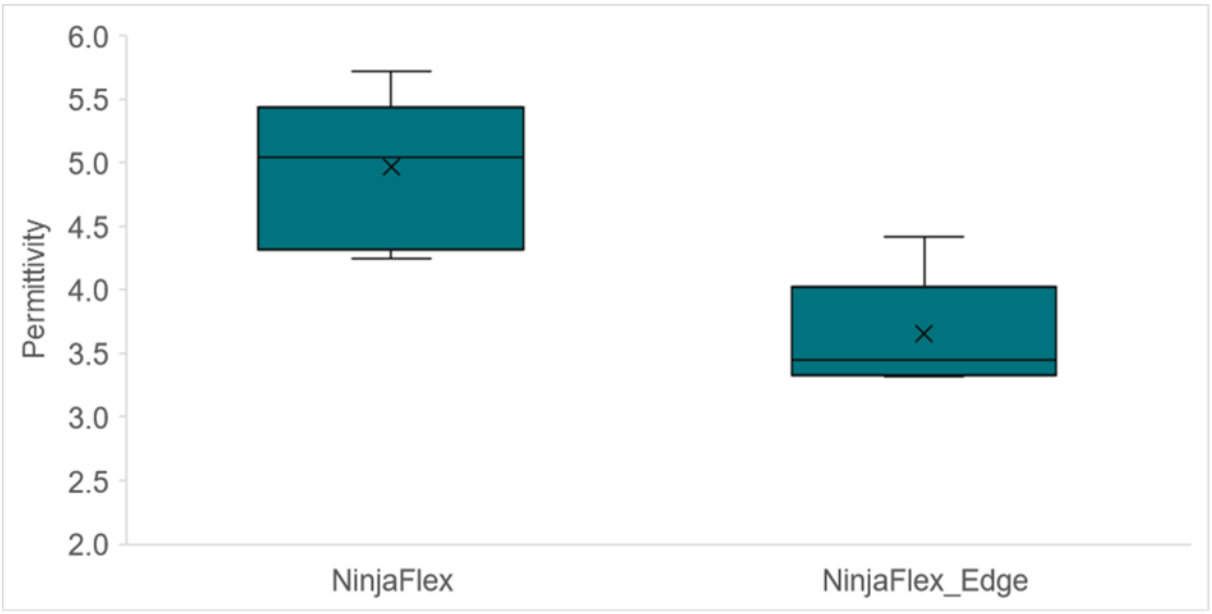

Figure 35: Relative permittivity for NinjaFlex and NinjaFlex_Edge.

5.5 Viscosity

Figure 36 clearly demonstrates the enhanced processability of Fenner Inc. latest TPU compared to NinjaFlex, as it exhibits significantly lower apparent viscosity. NinjaFlex_Edge has an average apparent viscosity of 784 ± 56 Pa·s, while NinjaFlex has an average apparent viscosity of 1971 ± 336 Pa·s. This represents a reduction of approximately 40%.

It is important to emphasise that this measurement refers only to the apparent viscosity. To achieve more precise outcomes, it is necessary to use the Rabinowitsch correction to obtain more accurate shear rates, as well as the Bagley correction to correct any inlet pressure loss.

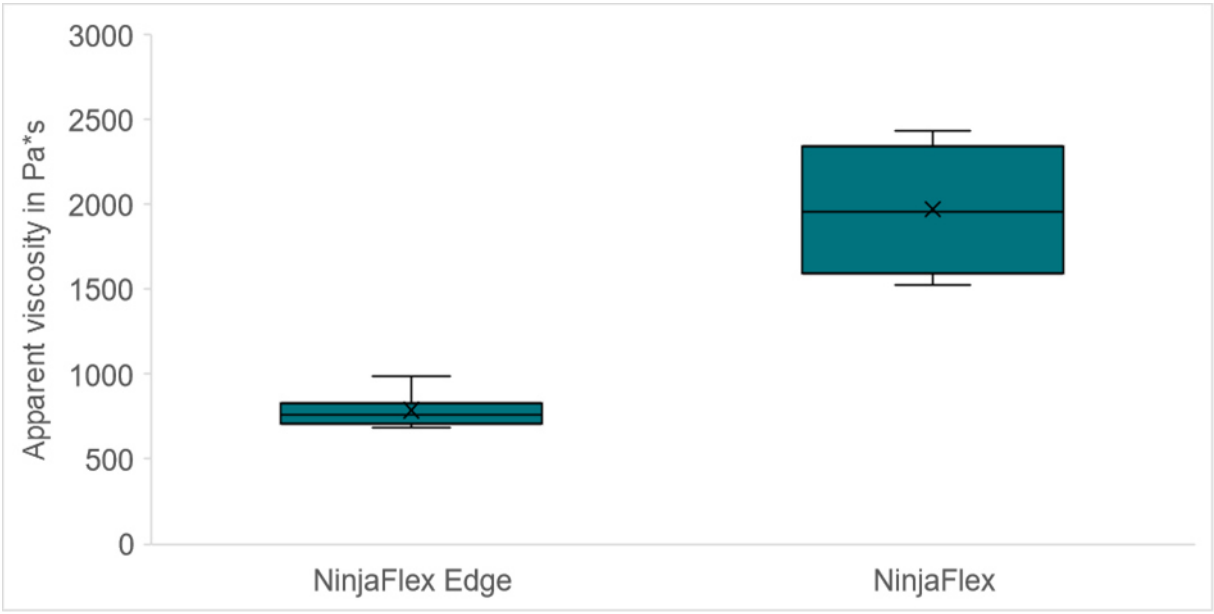

Figure 36:Apparent viscosity of NinjaFlex_Edge and NinjaFlex.

Another noteworthy observation was made during the measurements. During the three tests conducted with a single cylinder filling, the residence time consistently increased until the final measurement. Figure 37 clearly illustrates a pressure drop over time, resulting in a decrease in apparent viscosity. This was especially noticeable with NinjaFlex.

Nevertheless, since the melted material spends a short amount of time in the nozzle, this phenomenon does not impact the processing. Regardless of the temperature of the inactive toolhead, the nozzle will still be purged before printing continues.

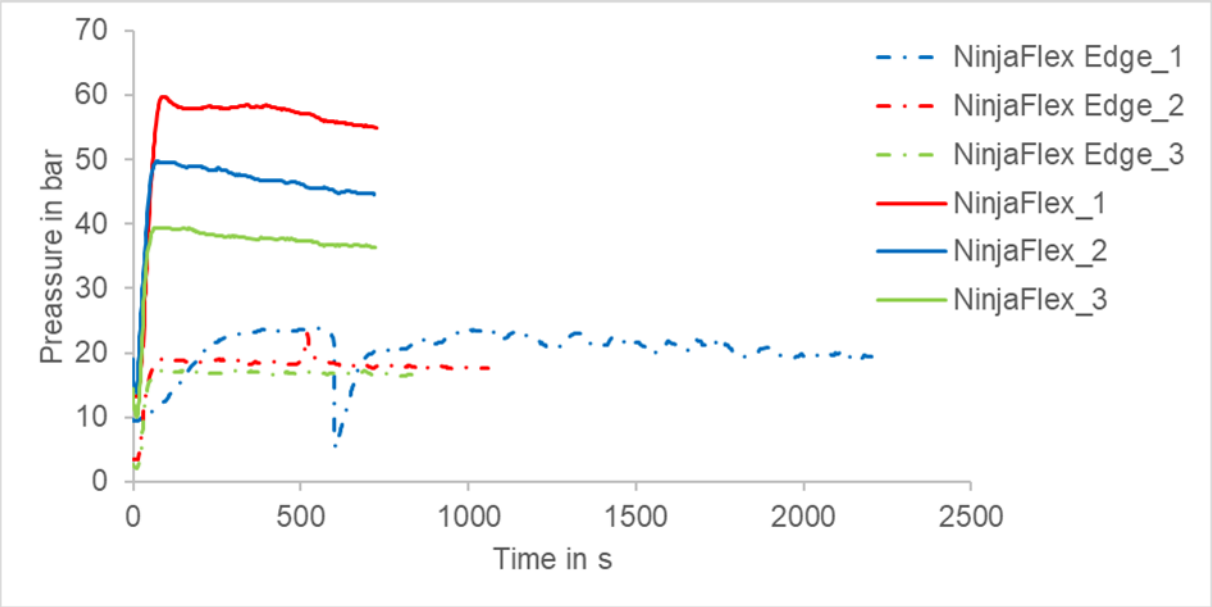

Figure 37: Viscosity measurements of NinjaFlex_Edge and NinjaFlex at constant speed.

5.6 Actuator

The actuators were sequentially printed in various combinations. Hence, these results were aggregated for each group in order to enhance the representation of reproducibility. The results for FiberFlex40D were excluded from the section due to insufficient applied force to induce displacement on the actuator before failure. Additionally, the high adhesion on the print bed caused minor damage to the actuators, resulting in the inability to produce valid results.

5.6.1 Printing Accuracy

To verify the precision of the custom-built printer, the most straightforward approach is to measure the thickness of the actuator and determine if the desired height has been achieved. Figure 38 displays the measured thickness. The results indicate fluctuations both above and below the targeted part thickness. This primarily concerns a hardware problem, which is elaborated upon in section 6. The maximum deviation from the average value is approximately 8 %, which is a satisfactory outcome given the quality of the printer's used parts.

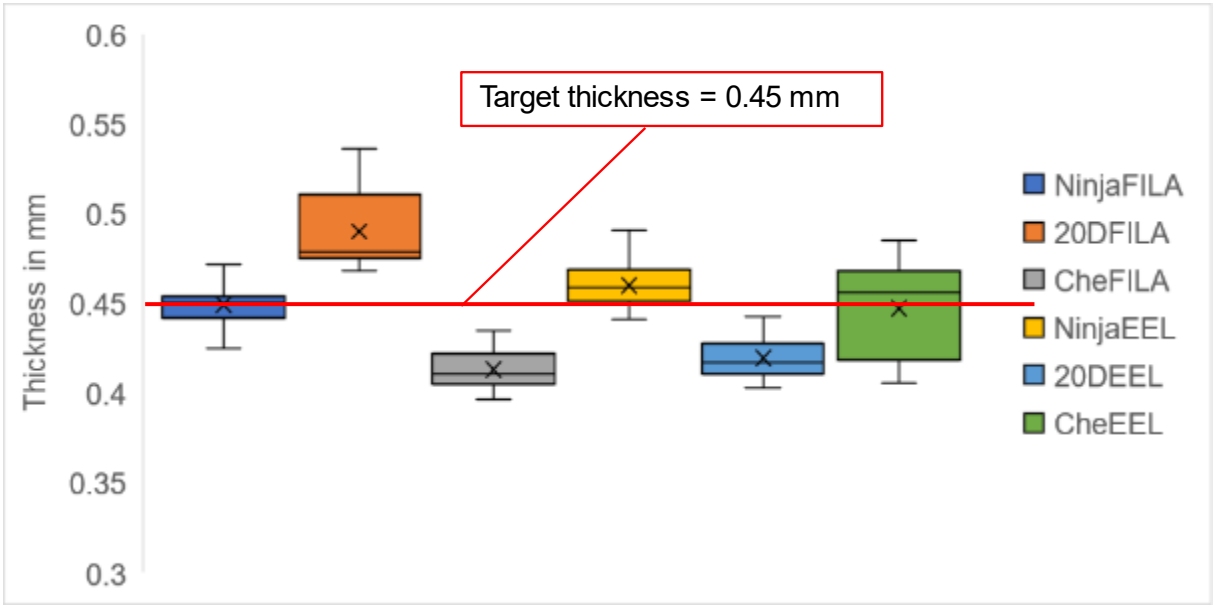

Figure 38: Thickness distribution of the actuators including target thickness of 0.45 mm.

However, in order to determine whether the membrane inside the actuator has the correct thickness, the capacitance is measured. The theoretical capacitance was calculated using the previously determined permittivity and then compared with the measurements. Figure 39 displays the outcomes of the capacitance measurements.

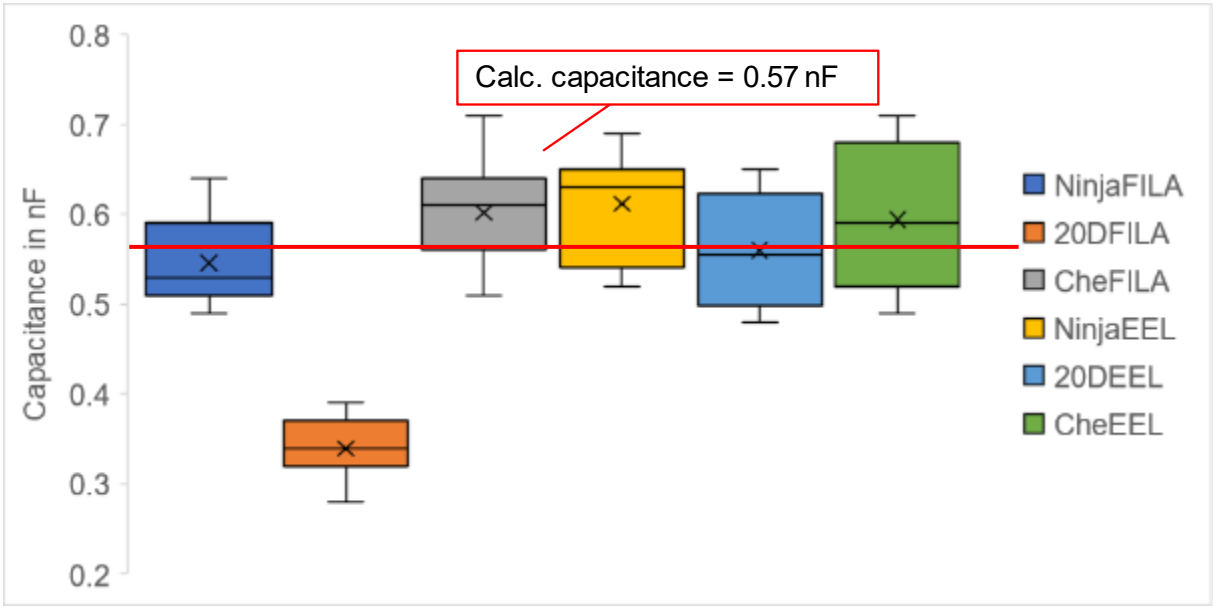

Figure 39: Capacitance distribution of the actuators including target capacitance of 0.51 nF.

The material combination 20DILA exhibits an apparent connection between the overall thickness of the part and its capacitance. It suggests that there is a substantial gap between both electrodes, resulting in a reduction in capacitance, as depicted in Figure 39. By employing this approach, it is possible to establish a correlation between the thickness of the actuator and its capacity. It is important to mention that the capacitance was measured using a multimeter, indicating that the results may not be completely precise.

5.6.2 Displacement

In order to obtain a more comprehensive understanding of the results from the displacement measurements, actuator configurations with the same passive layers but different electrode materials were compared. The test specimen was fixed on one side, causing it to operate in a manner similar to a cantilever. The displacement was measured manually using a grid, in each instance after incrementing the voltage by 0.2 V until reaching a maximum of 6 kV (shown in Figure 40).

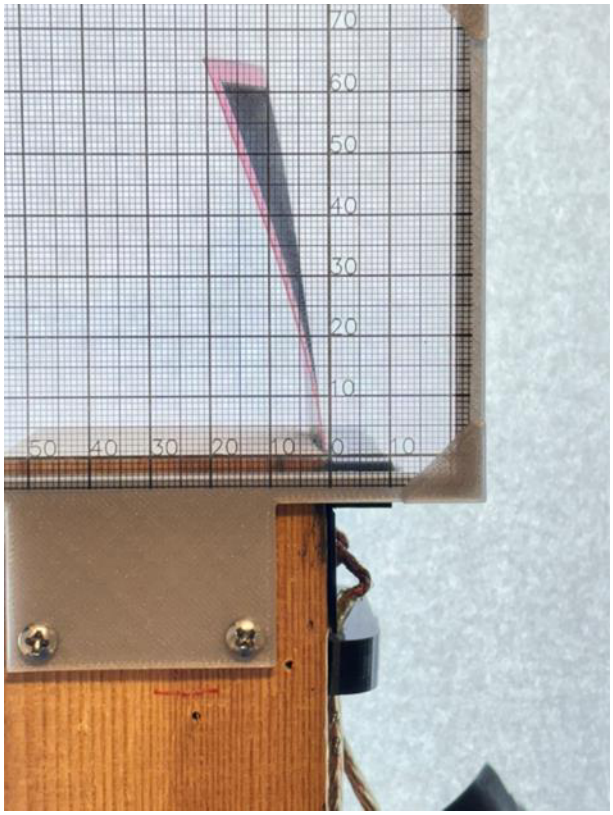

Figure 40: Measurement setup for displacement.

Figure 41 displays the displacement of the actuators, which consist primarily of just two distinct materials. The passive layer and the membrane are composed of identical materials. There was no apparent disparity in displacement. However, there is a variation in the measured values for the capacitance. Once again, this measurement was taken using a multimeter, so the accuracy is not guaranteed. Despite certain inaccuracies in the capacitance measurement, there is a noticeable correlation between capacitance and maximal displacements. Generally, higher capacitance tends to result in larger displacements, with a few exceptions.

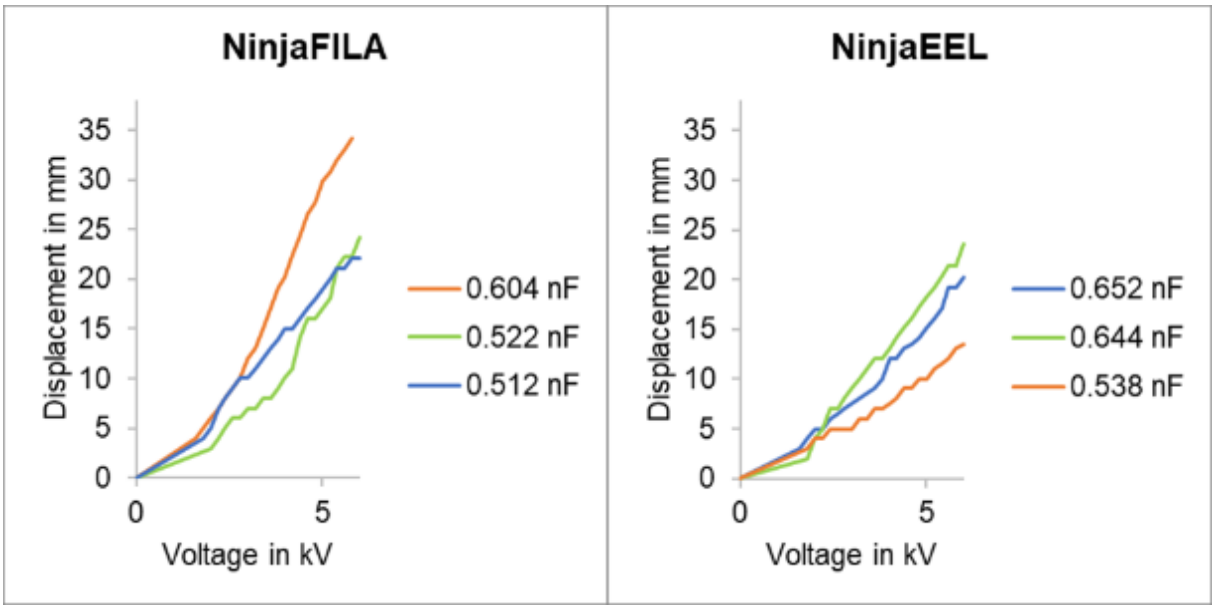

Figure 41: Displacement measurements of the actuator combinations NinjaFILA and NinjaEEL.

The significant variation in the desired thicknesses for the actuator combination 20DFILA, as stated in section 5.6.1, is also apparent in the significantly reduced displacement depicted in Figure 42. The capacitor with the lowest capacitance exhibited minimal displacement until it approached a voltage of approximately 5 kV, at which point it underwent a sudden and significant rise.

During the tests, one specimen of 20DEEL experienced a short circuit and was consequently not included in the diagram. It demonstrates that even a small deviation from the optimal thickness can result in diminished performance of the actuator or even a total breakdown.

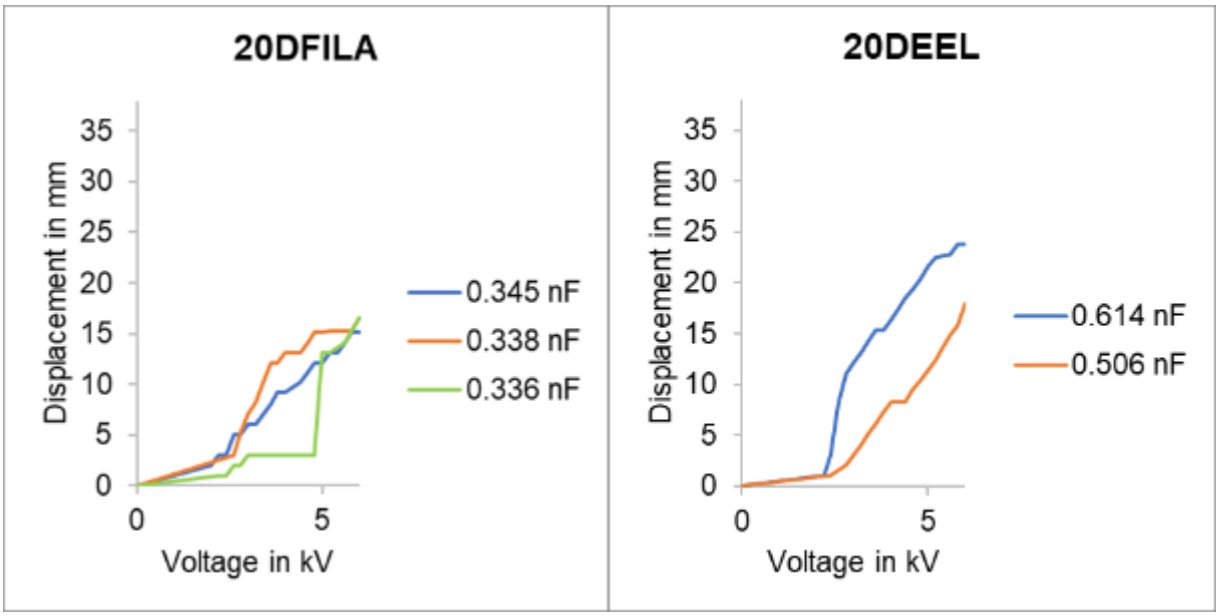

Figure 42: Displacement measurements of the actuator combinations 20DFILA and 20DEEL.

The actuator configuration Cheetah, with its passive layer, generated the most optimal outcomes (shown in Figure 43). The CheFila combination achieved a maximum displacement

of 38 mm with a capacitance of 0.646 nF. All specimens showed a notable increase at approximately 2 kV, and the curve profiles of all specimens are closely similar.

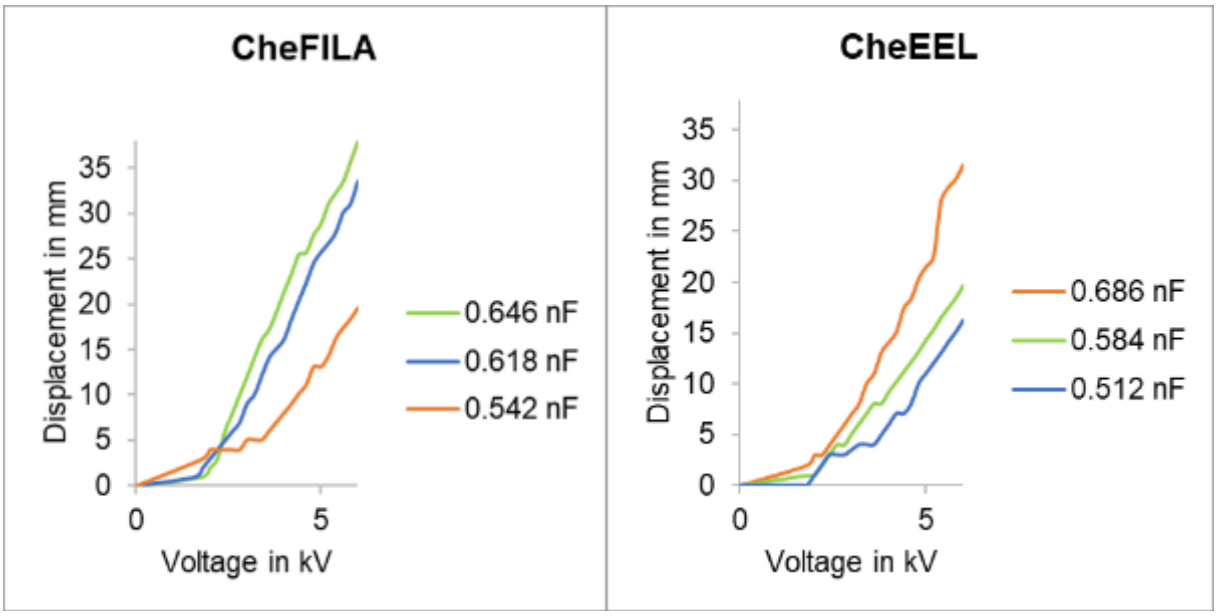

Figure 43: Displacement measurements of the actuator combinations CheFILA and CheEEL.

The variation among the actuators is evident in Figure 43. The displacement varies between 15 mm and 38 mm when the voltage is 6 kV. Many of the specimens may have the ability to withstand a higher voltage, resulting in a larger displacement. However, this specific maximum voltage was selected to guarantee a fair comparison with all printed components. The combinations involving NinjaFlex Eel™ exhibited slightly a reduced displacement as a result of its greater bending stiffness in comparison to FILAFLEX.

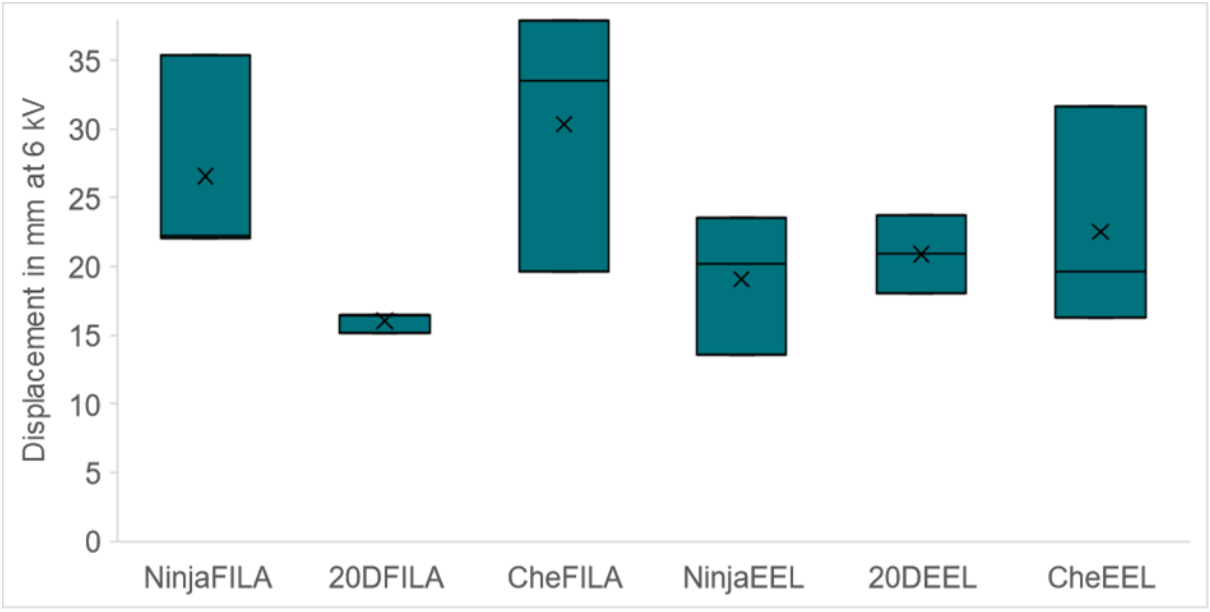

Figure 44: Maximum displacement of all actuator configurations at 6 kV.

Figure 45 depicts the path followed by the tip of the actuator combination NinjaEEL, demonstrating its movement. The origin represents the initial position where no voltage is applied. It is then increased in intervals of 0.2 kV until it reaches 6 kV. A second-degree polynomial trendline is used to accurately map the displacement.

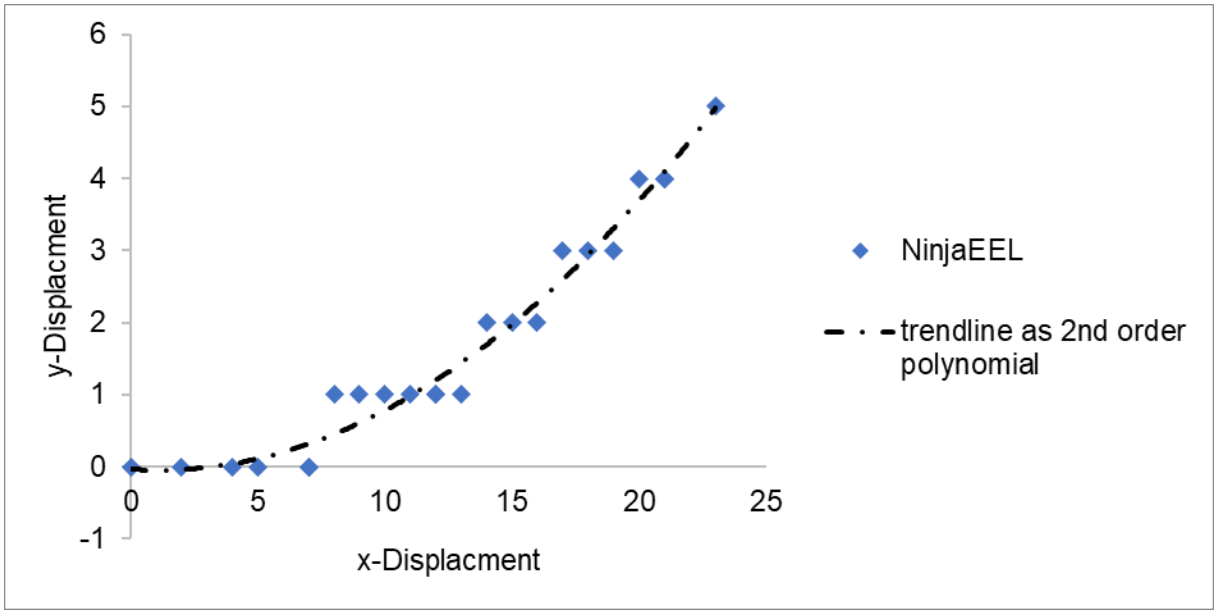

Figure 45: The trajectory of the leading point of the actuator combination NinjaEEL ranges from 0 to 6 kV, increasing in increments of 0.2 kV.

5.6.3 Three-finger Actuator

An example of a potential application for the actuators is a gripper arm that uses three or more actuators connected in parallel. Figure 45 depicts the configuration of the three-finger actuators. The individual actuators are interconnected by a thin conductor band (shown in Figure 45). There exists a slight distance between them, allowing for their arrangement in a triangular formation (Figure 46). A voltage is induced; in this instance, it is approximately four kilovolts. The fingers experience simultaneous movement and are capable of grasping an object.

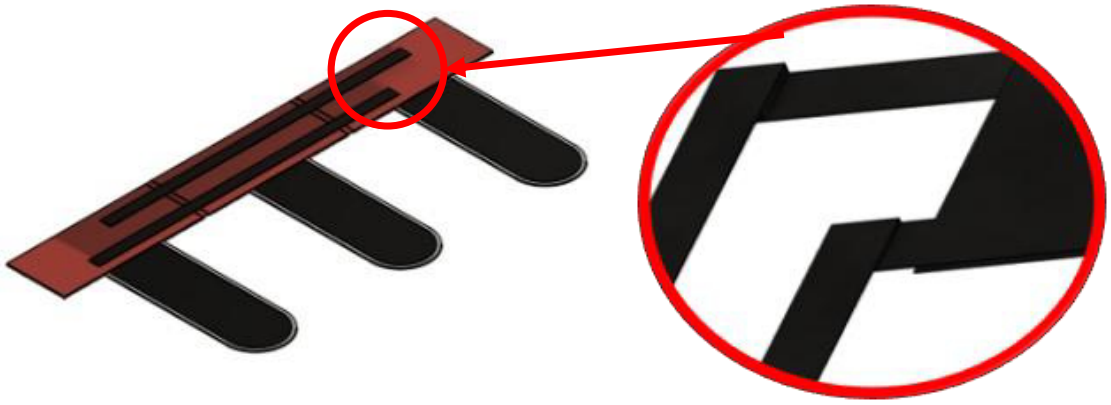

Figure 46: Design of the three-finger actuator with its conductor band connection.

A small polystyrene piece has been used to demonstrate the underlying operational principle. The object was wrapped in insulating tape to prevent the occurrence of electrostatic charges between the Styrofoam and the DEA. Figure 47 displays the sequential stages of the entire process.

Figure 47: Working principle of the three-finger actuator.

An unforeseen phenomenon occurred upon reaching a voltage of 5 kV. The fingers exhibited a repulsive force from each other. This phenomenon is likely caused by the individual electric fields of the bottom electrode, all of which possess identical charges. Consequently, these electric fields repel one another when a specific voltage is applied.

6 Conclusion and Outlook

The material investigations revealed that there is no substantial correlation between shore hardness and Young's modulus or flexural modulus in the tested TPU samples. Moreover, the result can differ significantly when the materials are heavily filled in comparison to their counterparts that are not filled. In addition, the Poisson's ratio of all the tested materials remained consistent, regardless of their hardness and printing orientation. This clearly illustrates that relying solely on the shore hardness of materials is not always a dependable approach when selecting materials for specific purposes, such as achieving bending stiffness.

The difficulty in handling the dielectric membrane was evident in the measurement of its viscosity. The high apparent viscosity presents difficulties for the extruder in terms of introducing the filament into the nozzle. Despite the new materials appearing to address those issues, the reduced permittivity of the new material renders it unsuitable as a dielectric membrane. This study did not investigate the cause of a lower relative dielectric constant. However, further research must be conducted, as high permittivity is a crucial characteristic of an actuator.

The displacement tests revealed comparable results, regardless of the varying hardness of the passive layer. The determining factor seems to be the flexural rigidity of the electrode material. The component's capacitance is a crucial characteristic that needs to be carefully preserved by following precise geometries, especially between the two electrodes. The main cause of the general disparity in displacement results can be attributed to the inaccurate printing process. In order to achieve greater performance, it is imperative to either increase the relative dielectric constant of the filaments or substantially decrease the bending stiffness of the actuator.

The concept of combining three actuators and connecting them in parallel may appear trivial. Carrying out this process is highly challenging. Reducing the size of the fingers in comparison to the tested actuator decreases the capacitance and may result in the actuator ceasing to function. Identifying the most effective configurations and dimensions to create a device that functions perfectly would have exceeded the scope of this thesis. However, the operational principle was demonstrated and has the potential to function as a gripping arm.

The primary objective of this thesis was to develop a 3D printer capable of producing a functional actuator using three distinct materials without the need for additional post-processing. The results demonstrated a dependable and replicable approach to achieving this. The choice to employ two separate moving dual extruders along a single axis was both cost-effective and feasible. In certain cases, there was a deviation of over 10 percent in compliance with the geometry of the components. The main problem lies in the hardware, as the printer was not specifically designed to handle layer heights that are only a few tens of a micrometer. Reducing the size of the print bed and replacing trapezoidal screws with recirculating ball screws would significantly decrease slip. While printing, the printer executes a process known as z-hopping, which involves raising the bed slightly to retract and then lowering it again to resume printing. Retraction is essential for ensuring high-quality prints by preventing material from leaking out of the nozzle. By initially moving the nozzle away from the component and then retracting it, the deposited layer is protected from being pulled off. An additional major improvement would involve the installation of servo motors to raise the idle nozzle of the dual carriage. This would provide a broad range of geometric liberties. At present, the printer has a restricted width, which is the distance between the two nozzles, to prevent the inactive nozzle from colliding with the object being printed.

This study explores novel possibilities for controlling the motion of the actuator by utilising three different materials without altering its geometry. It is feasible to selectively displace specific components of the actuator by utilizing the induced voltage. Regarding the actuator used, it is possible to print the front section with a less rigid material and the rear section with a more flexible material. Consequently, the deformation would initially occur only in the front tip of the actuator, and the entire actuator would deform only when the voltage was raised.

7 Literature

[1] Abdihamzehkolaei, A.; Ahad, M.T.; Siddique, Z.: Volume Resistivity of Viton Polymer under Thermal Aging, Polymers 13 (5), 2021, doi: 10.3390/polym13050773.

[2] ISO ASTM 52900: Additive manufacturing — General principles — Fundamentals and vocabulary, 01.11.2021

[3] Albach, M.: Elektrotechnik, Studium Elektrotechnik, Pearson, München, 2011

[4] antclabs: BLTouch V3.1 | antclabs, 2024, https://www.antclabs.com/bltouch-v3 (Retrieved on: 13.02.2024)

[5] Arduino Official Store: Arduino Mega 2560 Rev3, 2024, https://store.arduino.cc/products/arduino-mega-2560-rev3 (Retrieved on: 13.02.2024)

[6] Atakok, G.; Kam, M.; Koc, H.B.: Tensile, three-point bending and impact strength of 3D printed parts using PLA and recycled PLA filaments: A statistical investigation, Journal of Materials Research and Technology 18, 2022, pp. 1542–1554, doi: 10.1016/j.jmrt.2022.03.013.

[7] Aurilia, M.; Piscitelli, F.; Sorrentino, L.; Lavorgna, M.; Iannace, S.: Detailed analysis of dynamic mechanical properties of TPU nanocomposite: The role of the interfaces, European Polymer Journal 47 (5), 2011, pp. 925–936, doi: 10.1016/j.eurpolymj.2011.01.005.

[8] Bates, S.R.; Farrow, I.R.; Trask, R.S.: 3D printed polyurethane honeycombs for repeated tailored energy absorption, Materials & Design 112, 2016, pp. 172–183, doi: 10.1016/j.matdes.2016.08.062.

[9] Bauer, S.; Bauer-Gogonea, S.; Graz, I.; Kaltenbrunner, M.; Keplinger, C.; Schwödiauer, R.: 25th anniversary article: A soft future: from robots and sensor skin to energy harvesters, Advanced Materials 26 (1), 2014, pp. 149–161, doi: 10.1002/adma.201303349.

[10] Bhagia, S.; Bornani, K.; Agrawal, R.; Satlewal, A.; Ďurkovič, J.; Lagaňa, R.; Bhagia, M.; Yoo, C.G.; Zhao, X.; Kunc, V.; Pu, Y.; Ozcan, S.; Ragauskas, A.J.: Critical review of FDM 3D printing of PLA biocomposites filled with biomass resources, characterization, biodegradability, upcycling and opportunities for biorefineries, Applied Materials Today 24, 2021, pp. 101078, doi: 10.1016/j.apmt.2021.101078.

[11] Bigue, J.-P.L.; Plante, J.-S.: Experimental Study of Dielectric Elastomer Actuator Energy Conversion Efficiency, IEEE/ASME Transactions on Mechatronics 18 (1), 2013, pp. 169–177, doi: 10.1109/TMECH.2011.2164930.

[12] Blythe, A.R.; Bloor, D.: Electrical properties of polymers, 2. Ed., Cambridge Univ. Press, Cambridge, 2005

[13] Blythe, T.: Electrical properties of polymers, 1. Ed., Cambridge Univ. Press, Cambridge, 2008

[14] Bondtech: Bondtech LGX Large Gears eXtruder is smarter, smaller, lighter, 2024, https://www.bondtech.se/product/lgx-large-gears-extruder/ (Retrieved on: 06.02.2024)

[15] Bondtech: Bondtech LGX® Lite - Large Gears eXtruder w/ 36mm round stepper motor, 2024, https://www.bondtech.se/product/lgx-lite-large-gears-extruder/ (Retrieved on: 06.02.2024)

[16] Brochu, P.; Pei, Q.: Advances in dielectric elastomers for actuators and artificial muscles, Macromolecular rapid communications 31 (1), 2010, pp. 10–36, doi: 10.1002/marc.200900425.

[17] Carneiro, O.S.; Silva, A.F.; Gomes, R.: Fused deposition modeling with polypropylene, Materials & Design 83, 2015, pp. 768–776, doi: 10.1016/j.matdes.2015.06.053.
[18] Carpi, F.; Migliore, A.; Serra, G.; Rossi, D. de: Helical dielectric elastomer actuators, Smart Materials and Structures 14 (6), 2005, pp. 1210–1216, doi: 10.1088/0964-1726/14/6/014.
[19] Chua, C.K.; Leong, K.F.: 3D printing and additive manufacturing, Principles and applications, 5. Ed., World Scientific, New Jersey, London, Singapore, Beijing, Shanghai, Hong Kong, Taipei, Chennai, Tokyo, 2017
[20] Conrad, S.; Speck, T.; Tauber, F.J.: Tool changing 3D printer for rapid prototyping of advanced soft robotic elements, Bioinspiration & biomimetics 16 (5), 2021, doi: 10.1088/1748-3190/ac095a.
[21] CoreXY | Cartesian Motion Platform, 2012, https://corexy.com/theory.html (Retrieved on: 21.02.2024)
[22] Couch, M.; Binding, D.: High pressure capillary rheometry of polymeric fluids, Polymer 41 (16), 2000, pp. 6323–6334, doi: 10.1016/S0032-3861(99)00865-4.
[23] Cruz, S.M.; Viana, J.C.: Melt blending and characterization of carbon nanoparticles-filled thermoplastic polyurethane elastomers, Journal of Elastomers & Plastics 47 (7), 2015, pp. 647–665, doi: 10.1177/0095244314534097.
[24] Delebecq, E.; Pascault, J.-P.; Boutevin, B.; Ganachaud, F.: On the versatility of urethane/urea bonds: reversibility, blocked isocyanate, and non-isocyanate polyurethane, Chemical reviews 113 (1), 2013, pp. 80–118, doi: 10.1021/cr300195n.
[25] Dielectric Elastomers as Electromechanical Transducers, Fundamentals, materials, devices, models and applications of an emerging electroactive polymer technology, Elsevier, Amsterdam, 2008
[26] DIN EN ISO 18064:2022-08, Thermoplastische Elastomere_- Nomenklatur und Kurzzeichen (ISO_18064:2022); Deutsche Fassung EN_ISO_18064:2022
[27] DIN EN ISO 527-2:2012-06, Kunststoffe_- Bestimmung der Zugeigenschaften_- Teil_2: Prüfbedingungen für Form- und Extrusionsmassen (ISO_527-2:2012); Deutsche Fassung EN_ISO_527-2:2012
[28] DIN EN ISO/ASTM 52900:2022-03, Additive Fertigung_- Grundlagen_- Terminologie (ISO/ASTM 52900:2021); Deutsche Fassung EN_ISO/ASTM 52900:2021
[29] Duan, L.; D'hooge, D.R.; Spoerk, M.; Cornillie, P.; Cardon, L.: Facile and Low-Cost Route for Sensitive Stretchable Sensors by Controlling Kinetic and Thermodynamic Conductive Network Regulating Strategies, ACS applied materials & interfaces 10 (26), 2018, pp. 22678–22691, doi: 10.1021/acsami.8b03967.
[30] E3D: Bowden vs Direct Drive - What do I need in my 3D printer?, 2024, https://e3d-online.com/blogs/news/bowden-vs-direct-drive (Retrieved on: 27.03.2024)
[31] Ehrenstein, G.W.: Polymer-Werkstoffe, Struktur - Eigenschaften - Anwendung, Hanser eLibrary, 3. Ed., Hanser, München, 2011
[32] EPFL: Ultra-high voltage (7+ kV) power supply for dielectric elastomer actuators, 2023 (Retrieved on: 21.06.2023)
[33] Fiberlogy: FIBERFLEX 30D, 2023, https://fiberlogy.com/de/filamente/fiberflex-30d/ (Retrieved on: 29.02.2024)
[34] Fiberlogy: FIBERFLEX 40D, 2023, https://fiberlogy.com/de/filamente/fiberflex-40d/ (Retrieved on: 29.02.2024)
[35] Fischer, P.: Engineering Rheology - Second Edition, Applied Rheology 12 (1), 2002, pp. 10–11, doi: 10.1515/arh-2002-0019.

[36] Gibson, I.; Rosen, D.W.; Stucker, B.: Additive manufacturing technologies, 3D printing, rapid prototyping and direct digital manufacturing, Springer, New York [etc.], 2015
[37] Goldstein, H.; Poole, J.C.P.; Safko, S.J.L.: Klassische Mechanik, Lehrbuch Physik, 3. Ed., Wiley-VCH, Weinheim, 2012
[38] Grellmann, W.; Seidler, S.: Kunststoffprüfung, 2. Ed., Hanser, München, 2011
[39] Gu, G.-Y.; Gupta, U.; Zhu, J.; Zhu, L.-M.; Zhu, X.-Y.: Feedforward deformation control of a dielectric elastomer actuator based on a nonlinear dynamic model, Applied Physics Letters 107 (4), 2015, doi: 10.1063/1.4927767.
[40] Gu, G.-Y.; Zhu, J.; Zhu, L.-M.; Zhu, X.: A survey on dielectric elastomer actuators for soft robots, Bioinspiration & biomimetics 12 (1), 2017, pp. 11003, doi: 10.1088/1748-3190/12/1/011003.
[41] Guo, Y.; Liu, L.; Liu, Y.; Leng, J.: Review of Dielectric Elastomer Actuators and Their Applications in Soft Robots, Advanced Intelligent Systems 3 (10), 2021, doi: 10.1002/aisy.202000282.
[42] Hajiesmaili, E.; Clarke, D.R.: Dielectric elastomer actuators, Journal of Applied Physics 129 (15), 2021, doi: 10.1063/5.0043959.
[43] Hepburn, C.: Polyurethane Elastomers, Springer Netherlands, Dordrecht, 2000
[44] Hirai, T.; Sadatoh, H.; Ueda, T.; Kasazaki, T.; Kurita, Y.; Hirai, M.; Hayashi, S.: Polyurethane‐elastomer‐actuator, Die Angewandte Makromolekulare Chemie 240 (1), 1996, pp. 221‐229, doi: 10.1002/apmc.1996.052400121.
[45] Huang, B.; Li, M.; Mei, T.; McCoul, D.; Qin, S.; Zhao, Z.; Zhao, J.: Wearable Stretch Sensors for Motion Measurement of the Wrist Joint Based on Dielectric Elastomers, Sensors (Basel, Switzerland) 17 (12), 2017, doi: 10.3390/s17122708.
[46] Hullette, T.: Direct Drive vs Bowden Extruder: The Differences, All3DP, 2018
[47] Joy-it ARD-CNC-Kit1 Motortreiber kaufen, 2024, https://www.conrad.at/de/p/joy-it-ard-cnc-kit1-motortreiber-1646889.html?utm_campaign=affiliate&utm_content=dl_article&zanpid=11517_1707834206_fff7053faa7d4d4a79f28551c67c84cb&utm_source=awin&utm_medium=cpo&sv1=affiliate&sv_campaign_id=376257&awc=11517_1707834206_fff7053faa7d4d4a79f28551c67c84cb&utm_campaign=deeplink (Retrieved on: 13.02.2024)
[48] Jung, J.W.; Lee, J.-S.; Cho, D.-W.: Computer-aided multiple-head 3D printing system for printing of heterogeneous organ/tissue constructs, Scientific Reports 6, 2016, pp. 21685, doi: 10.1038/srep21685.
[49] Kaiser, W.: Kunststoffchemie für Ingenieure, Von der Synthese bis zur Anwendung, 3. Ed., Hanser Verlag, München, 2011
[50] Kavanagh, J.L.; Engwell, S.L.; Martin, S.A.: A review of laboratory and numerical modelling in volcanology, Solid Earth 9 (2), 2018, pp. 531–571, doi: 10.5194/se-9-531-2018.
[51] Kim, J.; Kim, J.W.; Kim, H.C.; Zhai, L.; Ko, H.-U.; Muthoka, R.M.: Review of Soft Actuator Materials, International Journal of Precision Engineering and Manufacturing 20 (12), 2019, pp. 2221–2241, doi: 10.1007/s12541-019-00255-1.
[52] Kožar, I.; Sulovsky, T.; Plovanić, M.; Božić, Ž.: Verification of a displacement model for three-point bending test, Procedia Structural Integrity 46, 2023, pp. 143–148, doi: 10.1016/j.prostr.2023.06.024.
[53] Krumm, D.; Schwanitz, S.; Odenwald, S.: spinfortec2022, Tagungsband zum 14. Symposium der Sektion Sportinformatik und Sporttechnologie der Deutschen

Vereinigung für Sportwissenschaft (dvs), Chemnitz 29. - 30. September 2022, Universitätsverlag Chemnitz, Chemnitz, 2022

[54] OENORM EN 527-2: Kunststoffe - Bestimmung der Zugeigenschaften, 15.05.2012

[55] DIN EN ISO 178: Kunststoffe_- Bestimmung der Biegeeigenschaften (ISO 178:2019), 01.08.2019

[56] Laureto, J.; Pearce, J.: Open Source Multi-Head 3D Printer for Polymer-Metal Composite Component Manufacturing, Technologies 5 (2), 2017, pp. 36, doi: 10.3390/technologies5020036.

[57] Lee, H.-G.; Kim, J.-G.: Volume and Surface Resistivity Measurement of Insulating Materials Using Guard-Ring Terminal Electrodes, Energies 13 (11), 2020, pp. 2811, doi: 10.3390/en13112811.

[58] Lee, Y.R.; Kwon, H.; Lee, D.H.; Lee, B.Y.: Highly flexible and transparent dielectric elastomer actuators using silver nanowire and carbon nanotube hybrid electrodes, Soft matter 13 (37), 2017, pp. 6390–6395, doi: 10.1039/C7SM01329A.

[59] Lepoivre, A.; Boyard, N.; Levy, A.; Sobotka, V.: Heat Transfer and Adhesion Study for the FFF Additive Manufacturing Process, Procedia Manufacturing 47, 2020, pp. 948–955, doi: 10.1016/j.promfg.2020.04.291.

[60] Li, L.; Zhu, R.; Zhou, Z.; Ren, J.: Modeling of a micropump membrane with electrostatic actuator, In: Xu H. (Ed.), 2010 2nd International Conference on Advanced Computer Control, (ICACC 2010) ; Shenyang, China, 27 - 29 March 2010, IEEE, Piscataway, NJ, 2010, pp. 630–632

[61] Li, W.; Liu, J.; Hao, C.; Jiang, K.; Xu, D.; Wang, D.: Interaction of thermoplastic polyurethane with polyamide 1212 and its influence on the thermal and mechanical properties of TPU/PA1212 blends, Polymer Engineering & Science 48 (2), 2008, pp. 249–256, doi: 10.1002/pen.20853.

[62] Liu, G.-S.; Xu, Y.-W.; Wang, Y.-C.; Wang, L.; Zhang, Y.-D.; Hang, T.; Chen, H.-J.; Xie, X.; Yang, B.-R.: Electrostatic assembly of ultraviolet-curable cellulose-coated silver nanowires as transparent electrodes for nanogenerator, Applied Physics Express 11 (7), 2018, pp. 75002, doi: 10.7567/APEX.11.075002.

[63] Low, S.-H.; Lau, G.-K.: Bi-axially crumpled silver thin-film electrodes for dielectric elastomer actuators, Smart Materials and Structures 23 (12), 2014, pp. 125021, doi: 10.1088/0964-1726/23/12/125021.

[64] Maltini, E.; Anese, M.: Evaluation of viscosities of amorphous phases in partially frozen systems by WLF kinetics and glass transition temperatures, Food Research International 28 (4), 1995, pp. 367–372, doi: 10.1016/0963-9969(95)00006-8.

[65] Marn, J.; Delic, M.; Zunic, Z.: Non-Newtonian Fluid Flow Analysis with Finite Difference and Finite Volume Numerical Models, Applied Rheology 11 (6), 2001, pp. 325–335, doi: 10.1515/arh-2001-0019.

[66] Martin, D.J.; Meijs, G.F.; Gunatillake, P.A.; McCarthy, S.J.; Renwick, G.M.: The effect of average soft segment length on morphology and properties of a series of polyurethane elastomers. II. SAXS-DSC annealing study, Journal of Applied Polymer Science 64 (4), 1997, pp. 803–817, doi: 10.1002/(SICI)1097-4628(19970425)64:4<803::AID-APP20>3.0.CO;2-T.

[67] Material Extrusion | Additive Manufacturing Research Group | Loughborough University, 2023, https://www.lboro.ac.uk/research/amrg/about/the7categoriesofadditivemanufacturing/materialextrusion/ (Retrieved on: 25.03.2024)

[68] Mezger, T.: Das Rheologie Handbuch, Für Anwender von Rotations- und Oszillations-Rheometern, FARBE UND LACK / BIBLIOTHEK, 5. Ed., Vincentz Network, Hannover, 2016
[69] Mi, H.-Y.; Salick, M.R.; Jing, X.; Jacques, B.R.; Crone, W.C.; Peng, X.-F.; Turng, L.-S.: Characterization of thermoplastic polyurethane/polylactic acid (TPU/PLA) tissue engineering scaffolds fabricated by microcellular injection molding, Materials science & engineering. C, Materials for biological applications 33 (8), 2013, pp. 4767–4776, doi: 10.1016/j.msec.2013.07.037.
[70] Miller, J.A.; Lin, S.B.; Hwang, K.K.S.; Wu, K.S.; Gibson, P.E.; Cooper, S.L.: Properties of polyether-polyurethane block copolymers: effects of hard segment length distribution, Macromolecules 18 (1), 1985, pp. 32–44, doi: 10.1021/ma00143a005.
[71] NETZSCH - Analyzing and Testing. Leading in Thermal Analysis, Rheology and Fire Testing: Quantifying Shear Thinning Behavior on a Rotational Rheometer Using the Power Law Model, 2024, https://analyzing-testing.netzsch.com/en/application-literature/quantifying-shear-thinning-behavior-on-a-rotational-rheometer-using-the-power-law-model (Retrieved on: 25.03.2024)
[72] NinjaTek: Cheetah 3D Printer Filament (95A) - NinjaTek, 2021, https://ninjatek.com/shop/cheetah/ (Retrieved on: 29.02.2024)
[73] NinjaTek: Eel 3D Printer Filament (90A) - NinjaTek, 2021, https://ninjatek.com/shop/eel/#tech-specs (Retrieved on: 27.02.2024)
[74] NinjaTek: NinjaFlex 3D Printer Filament (85A) - NinjaTek, 2021, https://ninjatek.com/shop/ninjaflex/ (Retrieved on: 29.02.2024)
[75] NinjaTek: NinjaFlex Edge 3D Printer Filament (83A) - NinjaTek, 2022, https://ninjatek.com/shop/edge/ (Retrieved on: 29.02.2024)
[76] O'Halloran, A.; O'Malley, F.; McHugh, P.: A review on dielectric elastomer actuators, technology, applications, and challenges, Journal of Applied Physics 104 (7), 2008, doi: 10.1063/1.2981642.
[77] Pahl, M.H.; Gleißle, W.; Laun, H.M.; Pahl, M.; Laun, H.-M.: Praktische Rheologie der Kunststoffe und Elastomere, Kunststofftechnik, 4. Ed., VDI-Verl., Düsseldorf, 1995
[78] Pelrine, R.; Kornbluh, R.; Joseph, J.; Heydt, R.; Pei, Q.; Chiba, S.: High-field deformation of elastomeric dielectrics for actuators, Materials Science and Engineering: C 11 (2), 2000, pp. 89–100, doi: 10.1016/S0928-4931(00)00128-4.
[79] Pelrine, R.; Kornbluh, R.; Pei, Q.; Joseph, J.: High-speed electrically actuated elastomers with strain greater than 100%, Science 287 (5454), 2000, pp. 836–839, doi: 10.1126/science.287.5454.836.
[80] Peng, Q.; Wei, H.; Qin, Y.; Lin, Z.; Zhao, X.; Xu, F.; Leng, J.; He, X.; Cao, A.; Li, Y.: Shape-memory polymer nanocomposites with a 3D conductive network for bidirectional actuation and locomotion application, Nanoscale 8 (42), 2016, pp. 18042–18049, doi: 10.1039/C6NR06515E.
[81] Prusa3D by Josef Prusa: Original Prusa MMU3 upgrade kit (for MK3S+) | Original Prusa 3D printers directly from Josef Prusa, 2024, https://www.prusa3d.com/product/original-prusa-mmu3-upgrade-kit-for-mk3s-2/?gad_source=1&gclid=CjwKCAiArfauBhApEiwAeoB7qDrvbfj7IGQKzSqFpRmWIy4SfYoXaFTRF128F0ahZzhj9SA2mlGuSBoCRPIQAvD_BwE (Retrieved on: 27.02.2024)
[82] Pschaid, C.: HAGE 3Dp-A2 Betriebsanleitung, 2017
[83] Recreus: Flexibles Filament Conductive Filaflex, 2024, https://recreus.com/de/filamente/3-filaflex-conductivo.html (Retrieved on: 27.02.2024)

[84] Richert, P.: Kräfte im elektrischen Feld, 2021, http://ktet.fh-muenster.de/lehre/gde_3.htlatex/gde_3se5.html (Retrieved on: 21.02.2024)
[85] Rodrigues Carneiro, L.R.; Tavares, J.J.-P.Z.d.S.: Design and implementation of 3D printer for Mechanical Engineering Courses, International Journal for Innovation Education and Research 9 (3), 2021, pp. 293–312, doi: 10.31686/ijier.vol9.iss3.3001.
[86] Roels, E.; Terryn, S.; Iida, F.; Bosman, A.W.; Norvez, S.; Clemens, F.; van Assche, G.; Vanderborght, B.; Brancart, J.: Processing of Self-Healing Polymers for Soft Robotics, Advanced Materials 34 (1), 2022, e2104798, doi: 10.1002/adma.202104798.
[87] Rosset, S.; Shea, H.R.: Flexible and stretchable electrodes for dielectric elastomer actuators, Applied Physics A 110 (2), 2013, pp. 281–307, doi: 10.1007/s00339-012-7402-8.
[88] Rus, D.; Tolley, M.T.: Design, fabrication and control of soft robots, Nature 521 (7553), 2015, pp. 467–475, doi: 10.1038/nature14543.
[89] Scarpello, M.L.; Kazani, I.; Hertleer, C.; Rogier, H.; Vande Ginste, D.: Stability and Efficiency of Screen-Printed Wearable and Washable Antennas, IEEE Antennas and Wireless Propagation Letters 11, 2012, pp. 838–841, doi: 10.1109/LAWP.2012.2207941.
[90] Schmitt, B.M.; Zirbes, C.F.; Bonin, C.; Lohmann, D.; Lencina, D.C.; Da Netto, A.C.S.: A Comparative Study of Cartesian and Delta 3D Printers on Producing PLA Parts, Materials Research 20 (suppl 2), 2017, pp. 883–886, doi: 10.1590/1980-5373-mr-2016-1039.
[91] Scholz, G.; Gehringer, M.: Thermoplastische Elastomere, Im Blickfang, De Gruyter STEM, De Gruyter, Berlin, Boston, 2021
[92] Schröder, T.: Rheologie der Kunststoffe, Theorie und Praxis, Hanser, München, 2018
[93] Shian, S.; Diebold, R.M.; Clarke, D.R.: Tunable lenses using transparent dielectric elastomer actuators, Optics express 21 (7), 2013, pp. 8669–8676, doi: 10.1364/OE.21.008669.
[94] Skylar-Scott, M.A.; Mueller, J.; Visser, C.W.; Lewis, J.A.: Voxelated soft matter via multimaterial multinozzle 3D printing, Nature 575 (7782), 2019, pp. 330–335, doi: 10.1038/s41586-019-1736-8.
[95] Spoerk, M.; Gonzalez-Gutierrez, J.; Sapkota, J.; Schuschnigg, S.; Holzer, C.: Effect of the printing bed temperature on the adhesion of parts produced by fused filament fabrication, Plastics, Rubber and Composites 47 (1), 2018, pp. 17–24, doi: 10.1080/14658011.2017.1399531.
[96] Spontak, R.J.; Patel, N.P.: Thermoplastic elastomers: fundamentals and applications, Current Opinion in Colloid & Interface Science 5 (5-6), 2000, pp. 333–340, doi: 10.1016/S1359-0294(00)00070-4.
[97] Stiny, L.: Grundwissen Elektrotechnik und Elektronik, Eine leicht verständliche Einführung : 117 Aufgaben mit Lösungswegen, Lehrbuch, 7. Ed., Springer Vieweg, Wiesbaden, Heidelberg, 2018
[98] Store, B.: BIGTREETECH BTT Octopus Pro V1.0/V1.1 For 3D Printer, 2024, https://biqu.equipment/collections/control-board/products/bigtreetech-octopus-pro-v1-0-chip-f446 (Retrieved on: 08.02.2024)
[99] Test Methods for DC Resistance or Conductance of Insulating Materials
[100] Tipler, P.A.: Physik, Für Wissenschaftler und Ingenieure, SpringerLink Bücher, 7. Ed., Springer Spektrum, Berlin, Heidelberg, 2015

[101] Types of printers and their differences | Prusa Knowledge Base, 2024, https://help.prusa3d.com/article/types-of-printers-and-their-differences_112464 (Retrieved on: 21.02.2024)
[102] What is TPE| KRAIBURG TPE, 2024, https://www.kraiburg-tpe.com/en/thermoplastic-elastomers (Retrieved on: 19.02.2024)
[103] Xometry, T.: Gantry System for 3D Printing: Advantages and Disadvantages, Xometry, 2023
[104] Xu, H.: 2010 2nd International Conference on Advanced Computer Control, (ICACC 2010) ; Shenyang, China, 27 - 29 March 2010, IEEE, Piscataway, NJ, 2010

8 List of Tables and Figures

8.1 Tables

8.2 Figures

9 Abbreviations

Abbreviations	Definition	Unit
A	Area	m^2
AM	Additive manufacturing	
AMF	Additive manufacturing file	
AgNWs	Silver nanowires	
b	Breite	m
c	Capacitance	F
CAD	Computer-aided design	
CNTs	Carbon nanotubes	
d	Plate distance	m
d_0	Origin distance	m
d_1	Diameter of electrode	m
DE	Dielectric elastomer	
DEA	Dielectric elastic actuator	
E	Activation energy	J
E	Electric field strength	V/m
F_e	Electrostatic force	N
F_m	Mechanical force	N
FDM™	Fused Deposition Modeling	
HPCR	High-Pressure Capillary Rheometer	
HS	Hard segment	
l	Length	m
J	Current density	A/m^2
MEX	Material extrusion	
n	Power law index	
Q	Electric charge	C
P	Power	W
PTFE	Polytetrafluoroethylene	
PU	Polyurethane	
R	Gas constant	J/K*mol
R	Electrical resistance	Ω
SS	Soft segment	

STL	Standard Triangulation Language	
T	Temperature	K
TPE	Thermoplastic elastomer	
TPU	Thermoplastic polyurethane	
U	Voltage	V
$\dot{V}$	Volumetric speed	mm^3/s
v_P	Piston speed	mm/s
w	Displacement	m
W_e	Electric energy	J
W_m	Mechanical energy	J
Y	Young's modulus	N/m^2
γ	Shear rate	1/s
ε	Strain	
ε_0	Permittivity of free space	F/m
ε_r	Relative dielectric constant	
ε	Electric field constant	F/m
η	Viscosity	Pa*s
η_∞	Infinite viscosity	Pa*s
μ	Poisson's ratio	
ρ	Volume resistivity	Ω*m
σ	Tension	N/m^2
τ	Shear stress	N/m^2
ψ	Film volume	m^3

10 Appendix

AI name	Percentage of thesis	Description
DeepL	8 %	Translation of Abstract Minor help for sentence formation
Grammarly	5 %	Assistance for grammatic